

# A class of new high-order finite-volume TENO schemes for hyperbolic conservation laws with unstructured meshes

Zhe Ji, Lin Fu<sup>a,b,\*</sup>

<sup>a</sup>*Department of Mechanical and Aerospace Engineering, The Hong Kong University of Science and Technology, Clear Water Bay, Kowloon, Hong Kong*

<sup>b</sup>*Department of Mathematics, The Hong Kong University of Science and Technology, Clear Water Bay, Kowloon, Hong Kong*

---

## Abstract

The recently proposed high-order TENO scheme [Fu et al., Journal of Computational Physics, 305, pp.333-359] has shown great potential in predicting complex fluids owing to the novel weighting strategy, which ensures the high-order accuracy, the low numerical dissipation, and the sharp shock-capturing capability. However, the applications are still restricted to simple geometries with Cartesian or curvilinear meshes. In this work, a new class of high-order shock-capturing TENO schemes for unstructured meshes are proposed. Similar to the standard TENO schemes and some variants of WENO schemes, the candidate stencils include one large stencil and several small third-order stencils. Following a strong scale-separation procedure, a tailored novel ENO-like stencil selection strategy is proposed such that the high-order accuracy is restored in smooth regions by selecting the candidate reconstruction on the large stencil while the ENO property is enforced near discontinuities by adopting the candidate reconstruction from smooth small stencils. The nonsmooth stencils containing genuine discontinuities are explicitly excluded from the final reconstruction, leading to excellent numerical stability. Different from the WENO concept, such unique sharp stencil selection retains the low numerical dissipation without sacrificing the

---

\*Corresponding author.

*Email addresses:* [jizhe.npu@gmail.com](mailto:jizhe.npu@gmail.com) (Zhe Ji), [linfu@ust.hk](mailto:linfu@ust.hk) (Lin Fu)

shock-capturing capability. The newly proposed framework enables arbitrarily high-order TENO reconstructions on unstructured meshes. For conceptual verification, the TENO schemes with third- to sixth-order accuracy are constructed. Without parameter tuning case by case, the performance of the proposed TENO schemes is demonstrated by examining a set of benchmark cases with broadband flow length scales.

*Keywords:* TENO, WENO, unstructured mesh, high-order scheme, low-dissipation scheme, compressible fluids, hyperbolic conservation law

---

## 1. Introduction

For computational fluid dynamics (CFD), one core research topic is to develop high-order stable numerical methods for solving the governing hyperbolic conservation laws, i.e. the Euler or Navier–Stokes equations. The solution complexity of this set of initial-boundary value PDEs resides at that discontinuities may appear even when the initial condition is sufficiently smooth [31]. The basic requirements for modern numerical methods are that the high-order accuracy is achieved for smooth flows and the solution monotonicity is preserved in the vicinity of discontinuities [63][56]. For more complex fluid simulations, the low-dissipation property is also essential such that the small-scale flow structures can be resolved with high fidelity [42][29][30].

For flows over complex geometries, the established high-order numerical methods include, e.g., the conventional finite-volume [62][55][14] method, the discontinuous Galerkin (DG) [9][10] method, and the flux-reconstruction (FR) [40][79] method. The finite-volume method typically relies on the data from multi-layer neighboring cells for the targeted high-order reconstruction. On the other hand, DG and FR methods can achieve high-order accuracy by deploying high-order polynomials within the mesh element. This compactness allows for a dramatic reduction of programming complexity and inter-node data transfer for high-performance parallel computing with unstructured meshes [85]. Therefore, for low-Mach flows, DG and FR methods are more and more popular for high-fidelity simulations, e.g. for large-eddy simulations (LES) [21][22][43] and direct numerical simulations (DNS) [11][57][33].

However, when high-Mach flows with shockwaves are concerned, the deployment of the shock-capturing concept in these frameworks becomes inevitable and challenging. For the DG and FR frameworks, the most popular choice is to introduce the artificial viscosity method [1][35][77][79] for its simplicity in terms of implementation. However, the performance of the artificial viscosity method is typically unsatisfactory and the built-in parameters need intensive case-by-case tuning. One alternative avenue is to resort to a hybrid strategy, which first detects the shockwaves based on a certain indicator and locally deploys the finite-volume shock-capturing concept, e.g. the Total Variation Diminishing (TVD) [76][75][74] method, the essentially non-oscillatory (ENO) [37] method, the weighted ENO (WENO) [49] method, and the Total Variation Bounding (TVB) [61] method.

In terms of the TVD-based schemes for unstructured meshes, Barth and Jespersen [4] propose a novel oscillation-free second-order scheme involving a limiter acting on a linear reconstruction polynomial. Venkatakrishnan [78] further improves it by making it differentiable and thus better convergence property for steady state solutions is obtained. To extend these limiters with high-order accuracy for smooth flows, Li and Ren [48] propose the so-called weighted biased averaging procedure (WBAP) limiter by employing non-linear weighting coefficients for the reconstruction and up to fourth-order accuracy on unstructured meshes is achieved. Michalak and Ollivier-Gooch [53] develop the accuracy preserving limiter for high-order accurate solution of the Euler equations, where fourth-order accuracy is achieved with minimal sacrifices in convergence properties comparing to existing second-order approaches.

However, when concerning even higher-order reconstruction, the further development of limiter-based shock-capturing schemes becomes incredibly cumbersome. Instead, the WENO paradigm [49], originating from the ENO concept [37], is able to provide arbitrarily high-order reconstruction and sharp shock-capturing capability within a unified framework. Different from ENO, WENO schemes utilize a weighted average of several low-order candidates to form the high-order reconstruction on the full stencil. The nonlinear weights are computed dynamically based on the smoothness indicators of candidate stencils such that the optimal accuracy order is restored asymptotically in

smooth regions and the ENO property is enforced near discontinuities. While great success has been achieved for applications on structured meshes with WENO schemes, it is, however, non-trivial to extend the WENO weighting procedure to unstructured meshes. The main issue is that, for some mesh typologies, the optimal linear weights may become negative inducing numerical instabilities or even do not exist [39][83][60]. One way to solve this issue is to decrease the targeted accuracy order on the combined large stencil to that of the small candidate stencils [8][17][18][50]. Alternatively, the central WENO (CWENO) schemes [46][47][7][12], which feature stencils of different sizes and tailored weighting strategy, can avoid these numerical difficulties since the choice of the linear weights can be arbitrary as long as their total sum equals one. The latest variants of CWENO schemes include the multi-resolution WENO schemes [87][88] and the WENO schemes with adaptive orders [2].

More recently, Fu et al. [26][27][28] propose a family of high-order targeted ENO (TENNO) schemes for solving the hyperbolic conservation laws. By introducing the novel ENO-like stencil selection strategy, the TENNO schemes feature low numerical dissipation and sharp shock-capturing property. Compared to WENO schemes, one unique property of TENNO is that the background linear scheme can be restored exactly for up to intermediate wavenumbers without sacrificing the robustness for capturing strong discontinuities. In this way, the performance of TENNO schemes can be well controlled by optimizing the spectral properties of the underlying background linear schemes. The TENNO-family schemes have been widely deployed to different complex fluid simulations on structured meshes, e.g. the multiphase flows [36], the detonation simulations [15], the magnetohydrodynamics (MHD) [32], the compressible gas dynamics [65][84][81][82][20], the turbulent flows [13][54][52][44][51], etc.

As far as the authors' knowledge, the high-order TENNO schemes have not been extended to the unstructured meshes, and consequently the applications are restricted to canonical simulations. In this work, a new class of high-order TENNO schemes on unstructured meshes are proposed. Similar to the idea in the standard TENNO schemes [26][27][28] and the WENO variants [46][7][86][3], the candidate stencils involve one large central-biased stencil and

several small directional stencils. A tailored novel ENO-like stencil selection strategy is proposed, which ensures that the final scheme is equipped with the high-order reconstruction on the large stencil in smooth regions and with the low-order reconstruction on small smooth stencils near the discontinuities. Except for the constant  $C_T$  in the weighting strategy, which separates the discontinuities from smooth scales in spectral space and can be determined by aprior analyses, no additional case-by-case empirical parameters are involved in the proposed TENO schemes. Moreover, arbitrarily high-order accurate TENO schemes can be constructed with this unified framework. For the conceptual demonstration, the TENO schemes with third- to sixth-order accuracy are constructed and validated with a set of critical benchmark simulations.

The remainder of this paper is organized as follows. (1) In section 2, the high-order finite-volume framework for solving the hyperbolic conservation laws is briefly reviewed as well as the WENO and CWENO reconstruction schemes; (2) In section 3, the new high-order TENO schemes for unstructured meshes are developed; (3) In section 4, the numerical method for flux evaluations is discussed; (4) In section 5, the performance of the proposed low-dissipation TENO schemes is demonstrated by conducting a wide range of critical benchmark simulations; (5) Conclusions and remarks are given in the last section.

## 2. Fundamentals of the unstructured finite-volume methods

In this section, the basic concepts of the unstructured finite-volume method including the classical high-order WENO and CWENO reconstruction schemes will be outlined.

### 2.1. Concepts of finite-volume method

For three-dimensional unsteady Euler equations, as typical hyperbolic conservation laws, the conservative form can be written as

$$\frac{\partial \mathbf{U}}{\partial t} + \nabla \cdot (\mathbf{F}(\mathbf{U})) = 0, \quad (1)$$

where  $\mathbf{U} = \mathbf{U}(\mathbf{x}, t)$  denotes the conservative variables and  $\mathbf{F}(\mathbf{U}) = (\mathbf{F}^x(\mathbf{U}), \mathbf{F}^y(\mathbf{U}), \mathbf{F}^z(\mathbf{U}))$  the nonlinear convection flux functions. Assuming that the computational

domain  $\Omega$  is partitioned by elements of various shapes, e.g. triangle, quadrilateral in 2D, or tetrahedral, hexahedral in 3D, integrating Eq. (1) over one control element  $\mathbb{I}_i$  results in the following semi-discrete form

$$\frac{d\bar{\mathbf{U}}_{\mathbb{I}_i}}{dt} = -\frac{1}{|V_{\mathbb{I}_i}|} \sum_j^{N_f} \sum_{\kappa}^{N_q} F^{\mathbf{n}_{\mathbb{I}_i,j}} \left( \mathbf{U}_{\mathbb{I}_i,j,L}^n(\mathbf{x}_{\mathbb{I}_i,j,\kappa}, t), \mathbf{U}_{\mathbb{I}_i,j,R}^n(\mathbf{x}_{\mathbb{I}_i,j,\kappa}, t) \right) \omega_{\kappa} |\mathbf{A}_{\mathbb{I}_i,j}|, \quad (2)$$

where  $\bar{\mathbf{U}}_{\mathbb{I}_i}$  is the volume-averaged conservative variable,  $V_{\mathbb{I}_i}$  the volume of control element  $\mathbb{I}_i$ ,  $N_f$  the cell face number of  $\mathbb{I}_i$ ,  $N_q$  the number of quadrature points deployed for the high-order surface integral approximation,  $F^{\mathbf{n}_{\mathbb{I}_i,j}}$  the numerical flux in the normal direction (pointing outwards) of face  $j$ ,  $\mathbf{U}_{\mathbb{I}_i,j,L}^n$  and  $\mathbf{U}_{\mathbb{I}_i,j,R}^n$  the left- and right-biased approximated solutions on the interface respectively,  $\omega_{\kappa}$  the weight for Gaussian integration point  $\mathbf{x}_{\mathbb{I}_i,j,\kappa}$ , and  $|\mathbf{A}_{\mathbb{I}_i,j}|$  the surface area of face  $j$ .

In order to advance the cell averages of the solution in time, the third-order strong-stability-preserving (SSP) Runge-Kutta method [34] is deployed for all the following investigations unless explicitly specified. The explicit formulas are given as

$$\begin{aligned} \bar{\mathbf{U}}_{\mathbb{I}_i}^{(1)} &= \bar{\mathbf{U}}_{\mathbb{I}_i}^n + \Delta t \mathcal{R}(\bar{\mathbf{U}}_{\mathbb{I}_i}^n), \\ \bar{\mathbf{U}}_{\mathbb{I}_i}^{(2)} &= \frac{3}{4} \bar{\mathbf{U}}_{\mathbb{I}_i}^n + \frac{1}{4} \bar{\mathbf{U}}_{\mathbb{I}_i}^{(1)} + \frac{1}{4} \Delta t \mathcal{R}(\bar{\mathbf{U}}_{\mathbb{I}_i}^{(1)}), \\ \bar{\mathbf{U}}_{\mathbb{I}_i}^{n+1} &= \frac{1}{3} \bar{\mathbf{U}}_{\mathbb{I}_i}^n + \frac{2}{3} \bar{\mathbf{U}}_{\mathbb{I}_i}^{(2)} + \frac{2}{3} \Delta t \mathcal{R}(\bar{\mathbf{U}}_{\mathbb{I}_i}^{(2)}), \end{aligned} \quad (3)$$

where  $\Delta t$  is the timestep size, and  $\mathcal{R}(\bar{\mathbf{U}}_{\mathbb{I}_i}^n)$  denotes the right hand side of Eq. (2).

Based on the standard finite-volume framework, the remaining numerical issue is to develop the high-order scheme to reconstruct the cell interface data, i.e.  $\mathbf{U}_{\mathbb{I}_i,j,L}^n(\mathbf{x}_{\mathbb{I}_i,j,\kappa}, t)$  and  $\mathbf{U}_{\mathbb{I}_i,j,R}^n(\mathbf{x}_{\mathbb{I}_i,j,\kappa}, t)$ , based on the known cell-averaged solutions, and to evaluate the cell interface flux  $F^{\mathbf{n}_{\mathbb{I}_i,j}} \left( \mathbf{U}_{\mathbb{I}_i,j,L}^n(\mathbf{x}_{\mathbb{I}_i,j,\kappa}, t), \mathbf{U}_{\mathbb{I}_i,j,R}^n(\mathbf{x}_{\mathbb{I}_i,j,\kappa}, t) \right)$ .

## 2.2. The high-order linear reconstruction schemes

Given a polynomial  $\mathcal{P}_{\mathbb{I}_i}(x, y, z)$  of order  $r$  in cell  $\mathbb{I}_i$ , if the reconstructed cell-averaged value equals  $\bar{\mathbf{U}}_{\mathbb{I}_i}$ , i.e.

$$\bar{\mathbf{U}}_{\mathbb{I}_i} = \frac{1}{|V_{\mathbb{I}_i}|} \int_{V_{\mathbb{I}_i}} \mathbf{U}(x, y, z) dV = \frac{1}{|V_{\mathbb{I}_i}|} \int_{V_{\mathbb{I}_i}} \mathcal{P}_{\mathbb{I}_i}(x, y, z) dV, \quad (4)$$

then  $r + 1$  order of accuracy is achieved. For unstructured meshes involving elements of various shapes, it is beneficial to transform all the elements from physical space ( $\mathbf{X} = (x, y, z)$ ) to a reference space ( $\mathbf{\Xi} = (\xi, \eta, \zeta)$ ) in order to reduce the scaling effects [18][17]. Following [73][71], all types of elements are first decomposed into basic elements of triangular or tetrahedral shape depending on the dimension of the problem. Then the coordinates of one of the new basic element are used as the reference to perform the transformation. Note that the spatial transformation does not change the cell-averaged solutions, i.e.

$$\bar{\mathbf{U}}_{\mathbb{I}_i} = \frac{1}{|V_{\mathbb{I}_i}|} \int_{V_{\mathbb{I}_i}} \mathbf{U}(x, y, z) dV \equiv \frac{1}{|V'_{\mathbb{I}_i}|} \int_{V'_{\mathbb{I}_i}} \mathbf{U}(\xi, \eta, \zeta) d\xi d\eta d\zeta. \quad (5)$$

For detailed descriptions, one is referred to [73][70].

To calculate reconstructed values in the targeted cell  $\mathbb{I}_0$ , a compact stencil  $\mathcal{S}$  is built with neighboring cells of  $\mathbb{I}_0$ . The amount of elements in  $\mathcal{S}$ , i.e.  $N_s$ , is determined by the total number of polynomial coefficients,  $N_k$ , which is calculated by

$$N_k = \frac{1}{n_d!} \prod_{m=1}^{n_d} (r + m), \quad (6)$$

where  $n_d$  is the number of dimension. In order to maintain good numerical stability with an acceptable computational cost, it is recommended to choose  $N_s = 2 \cdot N_k$  according to various studies [71][70][72], and we follow this setup for all the investigations in the present work.

The reconstruction polynomial  $\mathcal{P}(\xi, \eta, \zeta)$  can be expanded in  $\mathcal{S}$  over the local polynomial basis functions  $\psi_l(\xi, \eta, \zeta)$  as

$$\mathcal{P}(\xi, \eta, \zeta) = \sum_{l=0}^{N_k} a_l \psi_l(\xi, \eta, \zeta) = \bar{\mathbf{U}}_0 + \sum_{l=1}^{N_k} a_l \psi_l(\xi, \eta, \zeta), \quad (7)$$

where  $\bar{\mathbf{U}}_0$  denotes the cell-averaged solution of the target cell  $\mathbb{I}_0$ ,  $a_l$  the degrees of freedom to be calculated later. The basis functions  $\psi_l(\xi, \eta, \zeta)$  are defined as

$$\psi_l(\xi, \eta, \zeta) \equiv \varphi_l(\xi, \eta, \zeta) - \frac{1}{|V'_0|} \int_{V'_0} \varphi_l d\xi d\eta d\zeta, \quad l = 1, 2, \dots, N_k, \quad (8)$$

where

$$\varphi_l = \xi, \eta, \zeta, \xi^2, \eta^2, \zeta^2, \xi \cdot \eta, \dots, \quad (9)$$

to ensure that the constraint of Eq. (4) for the targeted cell  $\mathbb{I}_0$  is satisfied irrespective of choices of  $a_l$ .

Based on the constraint that the reconstructed cell-averaged values for all of the cells  $\mathbb{I}_s$  in  $\mathcal{S}$  should be equal to the corresponding cell-averaged solutions, one can obtain

$$\int_{V'_s} \mathcal{P}(\xi, \eta, \zeta) d\xi d\eta d\zeta = |V'_s| \bar{\mathbf{U}}_0 + \sum_{l=1}^{N_k} \int_{V'_s} a_l \psi_l(\xi, \eta, \zeta) d\xi d\eta d\zeta = |V'_s| \bar{\mathbf{U}}_s, \quad s = 1, \dots, N_s. \quad (10)$$

To find the unknown degrees of freedom  $a_l$ , Eq. (10) can be rewritten into

$$\sum_{l=1}^{N_k} \mathcal{A}_{sl} a_l = b_s, \quad s = 1, \dots, N_s, \quad (11)$$

where

$$\mathcal{A}_{sl} = \int_{V'_s} \psi_l(\xi, \eta, \zeta) d\xi d\eta d\zeta, \quad \text{and } b_s = |V'_s| (\bar{\mathbf{U}}_s - \bar{\mathbf{U}}_0). \quad (12)$$

The matrix  $\mathcal{A}_{sl}$  contains only the geometry information of each element in the considered stencil  $\mathcal{S}$ , and hence can be pre-calculated before the simulation. Since the matrix  $\mathcal{A}_{ls}^T \mathcal{A}_{sl}$  is invertible,  $a_l$  is obtained as

$$a_l = (\mathcal{A}_{ls}^T \mathcal{A}_{sl})^{-1} \mathcal{A}_{ls}^T b_s = \widehat{\mathcal{A}}_{ls} b_s, \quad (13)$$

where  $\widehat{\mathcal{A}}_{ls}$  can be further simplified by deploying a QR decomposition based on the Householder transformation [70][72] as

$$\widehat{\mathcal{A}}_{ls} = ((QR)^T(QR))^{-1} \mathcal{A}_{ls}^T = (R^T R)^{-1} \mathcal{A}_{ls}^T. \quad (14)$$

### 2.3. The high-order WENO reconstruction schemes

For a hyperbolic system, the above high-order linear reconstruction schemes are not suitable for handling discontinuities, such as shockwaves, presented in the computational domain. As in classical shock-capturing WENO schemes [41], the main idea is to obtain the high-order oscillation-free reconstruction based on a nonlinear convex combination of several candidate stencils. The

discontinuity can be captured sharply and stably by enforcing the ENO property through a nonlinear adaptation between the candidate reconstructions.

However, depending on the mesh typologies, the optimal linear weights may not exist for some circumstances [39][83][60]. To ensure the numerical robustness, the WENO scheme in [8][17][18][50] is considered, with which the targeted accuracy order of the combined reconstruction is identical to those of the candidate stencils.

Specifically, based on a set of candidate stencils  $(\mathcal{S}_0, \mathcal{S}_1, \dots, \mathcal{S}_K)$  with linear reconstructions  $\mathcal{P}_k(\xi, \eta, \zeta), k = 0, \dots, K$  featuring the same targeted accuracy order, the final nonlinearly combined WENO reconstruction is given as

$$\mathcal{P}^W(\xi, \eta, \zeta) = \sum_{k=0}^K w_k \mathcal{P}_k(\xi, \eta, \zeta), \quad (15)$$

where the nonlinear weight  $w_k$  is defined as

$$\omega_k = \frac{\alpha_k}{\sum_{k=0}^K \alpha_k}, \text{ and } \alpha_k = \frac{d_k}{(\beta_k + \varepsilon)^4}, \quad k = 0, \dots, K, \quad (16)$$

with  $\varepsilon = 10^{-14}$  and the smoothness indicators measured following the original definition in [41] as

$$\beta_k = \sum_{q=1}^r \oint_{V'_{i_0}} (\mathcal{D}^q \mathcal{P}_k(\xi, \eta, \zeta))^2 (d\xi, d\eta, d\zeta). \quad (17)$$

Since the optimal linear weights  $d_k$  are not designed to generate an even higher-order reconstruction scheme on the combined stencil, the values can be assigned flexibly. Previous investigations [8][17][18] reveal that the performance of the resulting WENO scheme can be improved by increasing the weight of the central-biased candidate stencil, which is less dissipative by construction. In practice, we set  $d_K = 10^4$  for the central-biased stencil  $\mathcal{S}_K$  and  $d_k = 1, k = 0, \dots, K - 1$  for the other directional stencils  $(\mathcal{S}_0, \mathcal{S}_1, \dots, \mathcal{S}_{K-1})$ , empirically.

Note that, all the linear candidate reconstructions  $\mathcal{P}_k(\xi, \eta, \zeta)$  of particular accuracy orders are constructed in the way described in the previous subsection, and satisfy the constraints of matching the cell-averaged solutions of

involved stencil cells. All of them are obtained by solving the overdetermined linear systems with the same constrained least-squares technique. Although there is a debate on which variable to be reconstructed by the WENO-type schemes, it is generally believed that the numerical oscillations can be better suppressed when the WENO reconstruction is carried out for characteristic variables than primitive or conservative variables [41][26].

#### 2.4. The high-order CWENO reconstruction schemes

In CWENO schemes [46][47][7][12], the candidate stencils include one large central-biased stencil  $\mathcal{S}_K$  and several small directional stencils ( $\mathcal{S}_0, \mathcal{S}_1, \dots, \mathcal{S}_{K-1}$ ), with which the high-order reconstruction scheme  $\mathcal{P}_K(\xi, \eta, \zeta)$  and the low-order reconstruction schemes  $\mathcal{P}_k(\xi, \eta, \zeta), k = 0, \dots, K-1$  are constructed, respectively. Note that, for good numerical robustness, the third-order reconstructions are adopted for small stencils. The most important ingredient of CWENO schemes is the introduction of an optimal reconstruction scheme as

$$\mathcal{P}^{\text{opt}}(\xi, \eta, \zeta) = \frac{1}{d_K} \left( \mathcal{P}_K(\xi, \eta, \zeta) - \sum_{k=0}^{K-1} d_k \mathcal{P}_k(\xi, \eta, \zeta) \right), \quad (18)$$

where the contributions of the lower-order reconstruction schemes are subtracted from the high-order reconstruction. Subsequently, the CWENO nonlinear scheme is given as a convex combination of the optimal candidate reconstruction scheme and other low-order candidate reconstruction schemes following

$$\mathcal{P}^{\text{CW}}(\xi, \eta, \zeta) = \frac{w_K}{d_K} \left( \mathcal{P}_K(\xi, \eta, \zeta) - \sum_{k=0}^{K-1} d_k \mathcal{P}_k(\xi, \eta, \zeta) \right) + \sum_{k=0}^{K-1} w_k \mathcal{P}_k(\xi, \eta, \zeta), \quad (19)$$

where  $w_k$  denotes the nonlinear weights and can be computed in a similar way as WENO schemes by

$$w_k = \frac{\alpha_k}{\sum_{k=0}^K \alpha_k}, \text{ and } \alpha_k = \frac{d_k}{(\beta_k + \varepsilon)^4}, \quad k = 0, \dots, K, \quad (20)$$

where  $\varepsilon = 10^{-14}$ . The smoothness indicator  $\beta_k$  is defined to be the same as that in WENO schemes. Unlike the WENO schemes, the linear weights  $d_k$

should satisfy

$$\sum_{k=0}^K d_k = 1, \text{ and } d_K = 1 - \frac{1}{d'_K}, \quad (21)$$

where  $d'_K$  can be taken arbitrarily and  $d_k$ ,  $k = 0, \dots, K - 1$  is calculated by

$$d_k = \frac{1 - d_K}{K}. \quad (22)$$

When the local flow scale is smooth,  $\omega_k \approx d_k$  and the high-order reconstruction is restored asymptotically with  $\mathcal{P}^{\text{CW}}(\xi, \eta, \zeta) \approx \mathcal{P}_K(\xi, \eta, \zeta)$ ; when approaching discontinuities, the contribution from the large candidate stencil will vanish and the smooth small stencils will dominate the final reconstruction. Therefore, the overall accuracy order of the resulting CWENO scheme is determined by the reconstruction scheme on the large stencil and the corresponding performance in nonsmooth regions is governed by the reconstruction schemes on the small stencils.

Increasing the optimal linear weight for large stencil can improve the wave-resolution property of the resulting CWENO scheme since the final scheme is biased to the high-order reconstruction. However, a too large value of  $d_K$  may also degrade the shock-capturing capability. In practice, we set  $d'_K = 10^4$ , i.e.,  $d_K = 1 - 10^{-4}$ , for the large stencil and  $d_k = \frac{10^{-4}}{K}$ ,  $k = 0, \dots, K - 1$  for the small directional stencils, empirically.

It is also worth noting that, to achieve the same accuracy order, the cost and complexity of the CWENO scheme are much smaller than the WENO scheme, since all the candidate stencils of WENO feature the same reconstruction order as the targeted order of the resulting nonlinear scheme. Also, the compactness of the small directional candidate stencils in CWENO increases the chance that at least one candidate is smooth in the high-gradient nonsmooth region and therefore enhances the numerical robustness when compared to WENO schemes.

### 3. The new class of high-order unstructured TENO reconstruction schemes

In this section, a new class of high-order unstructured TENO reconstruction schemes will be developed. The unstructured TENO weighting strategy

including the candidate stencil arrangement, the strong scale separation, the novel ENO-type stencil selection will be elaborated in detail.

### 3.1. The reconstruction candidate stencils

Similar to previous TENO [23] and CWENO [46] schemes, the core of the newly proposed unstructured TENO scheme is to design a set of candidate stencils involving both the large central-biased stencil and several small directional stencils. The desired overall high-order reconstruction scheme will be constructed based on the large central-biased stencil  $\mathcal{S}_K$  for resolving smooth scales, whereas a set of third-order reconstruction schemes will be constructed with the small directional stencils  $(\mathcal{S}_0, \mathcal{S}_1, \dots, \mathcal{S}_{K-1})$  for capturing discontinuities.

Fig. 1 shows the sketch of the central-biased and directional candidate stencils for the TENO6 scheme on different mesh typologies. In the present work, the central-biased stencil is built based on the Naive Cell based Algorithm (NCB) while the Type3 algorithm is employed to construct directional stencils following [70]. The stencil arrangement for unstructured meshes with other-type mesh elements follows a similar principle.

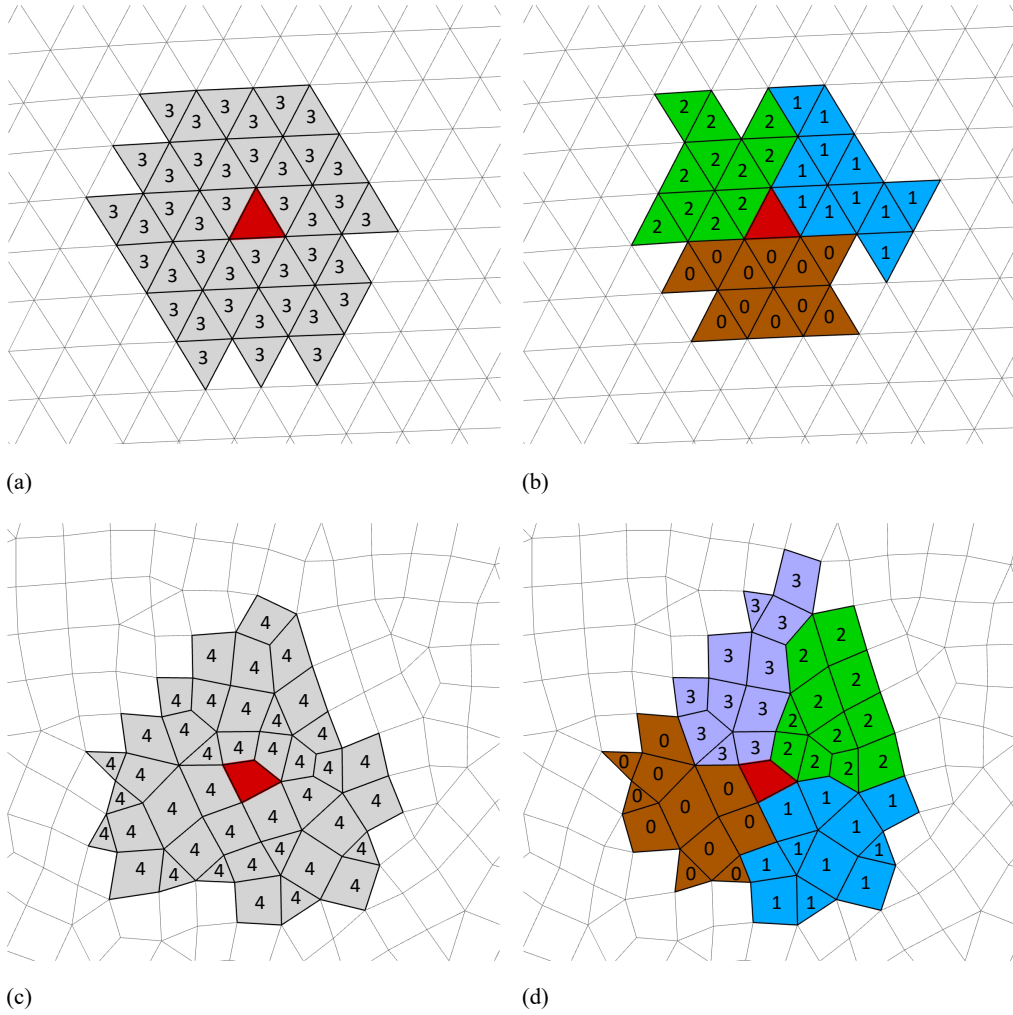


Figure 1: Sketch of (a) the sixth-order large central-biased candidate stencil  $\mathcal{S}_3$  and (b) the third-order small directional candidate stencils ( $\mathcal{S}_0, \mathcal{S}_1, \mathcal{S}_2$ ) for the TENO6 scheme on a triangular mesh; sketch of (c) the sixth-order large central-biased candidate stencil  $\mathcal{S}_4$  and (d) the third-order small directional candidate stencils ( $\mathcal{S}_0, \mathcal{S}_1, \mathcal{S}_2, \mathcal{S}_3$ ) for the TENO6 scheme on a mixed mesh. The index of each stencil is labelled in the figure and different stencils are filled with different colors. The cell considered for reconstruction  $\mathbb{I}_0$  is marked with red color.

### 3.2. Strong scale separation

Similar to that in the Cartesian TENO schemes [25][24], in order to isolate discontinuities from the smooth scales, one core algorithm of the TENO weighting strategy is to measure the smoothness of candidate stencils with strong scale separation as

$$\gamma_k = \frac{1}{(\beta_k + \varepsilon)^6}, \quad k = 0, \dots, K, \quad (23)$$

where  $\varepsilon = 10^{-12}$  is a small value to avoid the zero denominator and  $\beta_k$  denotes the smoothness function of candidate stencil  $k$  following Eq. (17) [41]. Compared to the classical WENO schemes [41], the exponent parameter is much larger for better scale separation and the low-dissipation property (which is difficult to achieve for WENO with this formula) will be retained by the following ENO-type stencil selection strategy. Note that, while the WENO-Z [6] type measurement can be applied here, it is not adopted for reducing the computational costs in the context of unstructured meshes and the previous investigation with the Cartesian TENO schemes [24] reveals that a similar scale-separation capability can be achieved with the present formula.

### 3.3. The new ENO-like stencil selection

In contrast to classical WENO schemes [41], where the contributions of the candidate stencils are combined in a smooth manner, for TENO, each stencil is explicitly judged to be a smooth or nonsmooth candidate by the so-called ENO-type stencil selection strategy. First, the measured smoothness indicator  $\chi_k$  is renormalized as

$$\chi_k = \frac{\gamma_k}{\sum \gamma_k}, \quad (24)$$

and then subjected to a sharp cut-off function

$$\delta_k = \begin{cases} 0, & \text{if } \chi_k < C_T, \\ 1, & \text{otherwise,} \end{cases} \quad (25)$$

where the parameter  $C_T$  determines the wavenumber, which separates the smooth and nonsmooth scales.

With the present stencil arrangement, the large central-biased candidate stencil  $\mathcal{S}_K$  features the highest accuracy order and the best spectral property and therefore is suitable for resolving the smooth flow scales. On the other hand, the set of small directional stencils is designed for capturing the possible discontinuity by a nonlinear adaptation among them. Specifically, the final data reconstruction on the cell interface can be determined in two steps as follows.

(i) Group all the candidate stencils as  $(\mathcal{S}_0, \mathcal{S}_1, \mathcal{S}_2, \dots, \mathcal{S}_K)$  and perform the ENO-type stencil selection following Eq. (24) and Eq. (25). If the largest candidate stencil  $\mathcal{S}_K$  is judged to be smooth, then the final reconstruction scheme is given as

$$\mathcal{P}^T(\xi, \eta, \zeta) = \mathcal{P}_K(\xi, \eta, \zeta); \quad (26)$$

(ii) If the largest candidate stencil  $\mathcal{S}_k$  is judged to be nonsmooth, then the nonlinear adaptation among the small stencils will be activated to capture the discontinuities by enforcing the ENO property, i.e. group all the small candidate stencils as  $(\mathcal{S}_0, \mathcal{S}_1, \mathcal{S}_2, \dots, \mathcal{S}_{K-1})$  and perform the ENO-type stencil selection following Eq. (24) and Eq. (25). The final reconstruction scheme is given as

$$\mathcal{P}^T(\xi, \eta, \zeta) = \sum_{k=0}^{K-1} w_k \mathcal{P}_k(\xi, \eta, \zeta), \quad (27)$$

where the nonlinear weight

$$w_k = \frac{\delta_k}{\sum_{k=0}^{K-1} \delta_k}, k = 0, 1, \dots, K - 1. \quad (28)$$

Note that, for both stencil selection steps, the parameter  $C_T$  is chosen to be the same, i.e.,  $C_T = 10^{-6}$ . Further optimization of the choice of  $C_T$  is beyond the scope of this paper and interested readers are referred to the discussions in [26][27][29].

### 3.4. Analysis and discussions

As demonstrated by previous investigations [26][27][28], the TENO weighting strategy can accurately identify the nonsmooth discontinuities from smooth flow scales. On the other hand, in smooth regions, the desirable high-order reconstruction will be restored exactly without any compromise. In other

words, in low-wavenumber regime, the nonlinear TENO scheme degenerates to the optimal linear scheme on the large stencil  $\mathcal{S}_K$ . In terms of resolving the small-scale features, such a property renders TENO schemes superior over WENO, for which the nonlinear adaptation (i.e., the nonlinear dissipation) is added even for low-wavenumber smooth regions.

Another notable property of the proposed unstructured TENO schemes is that neither the optimal linear weights  $d_k$  in WENO nor the artificial weights  $d'_k$  in CWENO schemes are necessary to specify, suggesting the highly general applicability.

#### 4. Numerical flux evaluations

In this section, we discuss the numerical method for flux evaluations to complete the spatial discretization under the finite-volume framework.

##### 4.1. Riemann problem definition

As proved in [67], based on the rotational invariance property, the following relation,

$$F^{\mathbb{m}_{i,j}}(\mathbf{U}) = \mathbf{T}_{\mathbb{I}_{i,j}}^{-1} \mathbf{F}^x(\mathbf{T}_{\mathbb{I}_{i,j}} \mathbf{U}), \quad (29)$$

where  $\mathbf{T}_{\mathbb{I}_{i,j}}$  denotes the unique rotation matrix for local cell face  $j$  of cell  $i$  (note that  $\mathbf{T}_{\mathbb{I}_{i,j}}$  is fixed for specific mesh topology), applies to the Euler equations, and the projected numerical flux can be further evaluated by

$$\mathbf{K}_{ij} = \sum_{\kappa}^{N_q} F^{\mathbb{m}_{i,j}} \left( \mathbf{U}_{\mathbb{I}_{i,j,L}}^n(\mathbf{x}_{\mathbb{I}_{i,j,\kappa}}, t), \mathbf{U}_{\mathbb{I}_{i,j,R}}^n(\mathbf{x}_{\mathbb{I}_{i,j,\kappa}}, t) \right) \omega_{\kappa} |\mathbf{A}_{\mathbb{I}_{i,j}}| = \sum_{\kappa}^{N_q} \mathbf{T}_{\mathbb{I}_{i,j}}^{-1} \mathbf{F}^x \left( \hat{\mathbf{U}}_L, \hat{\mathbf{U}}_R \right) \omega_{\kappa} |\mathbf{A}_{\mathbb{I}_{i,j}}|, \quad (30)$$

where the rotated variables are defined as

$$\hat{\mathbf{U}}_L = \mathbf{T}_{\mathbb{I}_{i,j}} \mathbf{U}_{\mathbb{I}_{i,j,L}}^n(\mathbf{x}_{\mathbb{I}_{i,j,\kappa}}, t), \quad \hat{\mathbf{U}}_R = \mathbf{T}_{\mathbb{I}_{i,j}} \mathbf{U}_{\mathbb{I}_{i,j,R}}^n(\mathbf{x}_{\mathbb{I}_{i,j,\kappa}}, t). \quad (31)$$

To close the spatial discretization, the remaining work reduces to evaluate the numerical flux  $\mathbf{F}^x(\hat{\mathbf{U}}_L, \hat{\mathbf{U}}_R)$  by solving the simple one-dimensional Riemann problem

$$\frac{\partial}{\partial t} \hat{\mathbf{U}} + \frac{\partial}{\partial s} \hat{\mathbf{F}}^x = \mathbf{0}, \quad \hat{\mathbf{F}}^x = \mathbf{F}^x(\hat{\mathbf{U}}), \quad \hat{\mathbf{U}}(s, 0) = \begin{cases} \hat{\mathbf{U}}_L, & s < 0, \\ \hat{\mathbf{U}}_R, & s > 0. \end{cases} \quad (32)$$

#### 4.2. HLL Riemman solver

Hereafter, the HLL [38][68] approximate Riemann solver, which has been demonstrated to be robust and reliable for Euler equations, is briefly reviewed. The approximate Riemann solution for the discontinuous left and right state  $\widehat{\mathbf{U}}_L, \widehat{\mathbf{U}}_R$  is

$$\tilde{\mathbf{U}}(x, t) = \begin{cases} \widehat{\mathbf{U}}_L, & \text{if } 0 \leq S_L, \\ \widehat{\mathbf{U}}^{hll}, & \text{if } S_L \leq 0, \\ \widehat{\mathbf{U}}_R, & \text{if } 0 \geq S_R, \end{cases} \quad (33)$$

and the corresponding flux is

$$\widehat{\mathbf{F}}_{i+\frac{1}{2}}^{hll,x} = \begin{cases} \widehat{\mathbf{F}}_L^x, & \text{if } 0 \leq S_L, \\ \frac{S_R \widehat{\mathbf{F}}_L^x - S_L \widehat{\mathbf{F}}_R^x + S_L S_R (\widehat{\mathbf{U}}_R - \widehat{\mathbf{U}}_L)}{S_R - S_L}, & \text{if } S_L \leq 0 \leq S_R, \\ \widehat{\mathbf{F}}_R^x, & \text{if } 0 \geq S_R. \end{cases} \quad (34)$$

where  $\widehat{\mathbf{F}}_L^x = \mathbf{F}^x(\widehat{\mathbf{U}}_L)$  and  $\widehat{\mathbf{F}}_R^x = \mathbf{F}^x(\widehat{\mathbf{U}}_R)$ . The acoustic wave-speed  $S_L$  and  $S_R$  are evaluated by [19][5]

$$S_L = \min(u_L - c_L, \tilde{u} - \tilde{c}), \quad S_R = \max(u_R + c_R, \tilde{u} + \tilde{c}), \quad (35)$$

where the Roe-averaged quantities are defined as

$$\begin{cases} D_\rho = \sqrt{\frac{\rho_R}{\rho_L}}, \\ \tilde{u} = \frac{u_L + u_R D_\rho}{1 + D_\rho}, \\ \tilde{H} = \frac{H_L + H_R D_\rho}{1 + D_\rho}, \\ \tilde{c} = \sqrt{(\gamma - 1)[\tilde{H} - \frac{1}{2}\tilde{u}^2]}. \end{cases} \quad (36)$$

## 5. Numerical validations

In this section, the proposed TENO schemes of third- to sixth-order are validated by solving the linear advection problem, the 1D and 2D Euler equations. If not mentioned otherwise, the third-order SSP Runge–Kutta scheme [34] is adopted for the temporal advancement with a constant CFL number 0.4. For all the simulations, the built-in parameters of TENO schemes

are fixed and the results from CWENO and WENO schemes are provided for comparisons. All the present schemes are implemented in the research platform [73][66][70], which has been extensively validated with both canonical and real-world simulations based on unstructured meshes.

### 5.1. Accuracy order tests

We consider the 2D linear advection equation

$$\frac{\partial u}{\partial t} + \frac{\partial u}{\partial x} + \frac{\partial u}{\partial y} = 0, \quad (37)$$

with the initial condition as

$$u(x, y, 0) = \sin(2\pi x) \cdot \sin(2\pi y). \quad (38)$$

Periodic condition is imposed for all boundaries and the simulation is run until  $t = 1$ .

As shown in Table 1, 2, 3, and 4, the desired accuracy order is restored for all the considered TENO schemes with respect to both the  $L^\infty$  and  $L^2$  norms. Moreover, the numerical truncation errors from the nonlinear TENO schemes are identical to those from the linear schemes for all the resolutions indicating that the targeted linear schemes are restored exactly.

Table 1: Accuracy order test for third order schemes

	$h$	$N_e$ <sup>1</sup>	$L^\infty$ error	$L^\infty$ order <sup>2</sup>	$L^2$ error	$L^2$ order
Linear	1/13	374	8.65E-02	-	4.58E-02	-
	1/20	918	2.37E-02	2.88	1.30E-02	2.81
	1/40	3674	3.33E-03	2.83	1.64E-03	2.98
	1/80	14860	3.78E-04	3.12	2.01E-04	3.01
	1/160	58330	5.14E-05	2.92	2.56E-05	3.01
TENO3	1/13	374	8.65E-02	-	4.58E-02	-
	1/20	918	2.37E-02	2.88	1.30E-02	2.81
	1/40	3674	3.33E-03	2.83	1.64E-03	2.98
	1/80	14860	3.78E-04	3.12	2.01E-04	3.01
	1/160	58330	5.14E-05	2.92	2.56E-05	3.01

<sup>1</sup> $N_e$  the total number of elements

<sup>2</sup>Both  $L^\infty$  and  $L^2$  order are calculated based on  $N_e$

Table 2: Accuracy order test for fourth order schemes

	$h$	$N_e$	$L^\infty$ error	$L^\infty$ order	$L^2$ error	$L^2$ order
Linear	1/13	374	7.99E-03	-	3.52E-03	-
	1/20	918	2.26E-03	2.81	8.29E-04	3.22
	1/40	3674	9.05E-05	4.64	3.28E-05	4.66
	1/80	14860	6.59E-06	3.75	2.15E-06	3.90
	1/160	58330	5.60E-07	3.61	1.57E-07	3.83
TEN04	1/13	374	7.99E-03	-	3.52E-03	-
	1/20	918	2.26E-03	2.81	8.29E-04	3.22
	1/40	3674	9.05E-05	4.64	3.28E-05	4.66
	1/80	14860	6.59E-06	3.75	2.15E-06	3.90
	1/160	58330	5.60E-07	3.61	1.57E-07	3.83

Table 3: Accuracy order test for fifth order schemes

	$h$	$N_e$	$L^\infty$ error	$L^\infty$ order	$L^2$ error	$L^2$ order
Linear	1/13	374	9.16E-03	-	4.80E-03	-
	1/20	918	1.06E-03	4.80	5.58E-04	4.79
	1/40	3674	3.43E-05	4.95	1.59E-05	5.13
	1/80	14860	9.68E-07	5.11	4.95E-07	4.97
	1/160	58330	3.33E-08	4.93	1.61E-08	5.01
TEN05	1/13	374	9.16E-03	-	4.80E-03	-
	1/20	918	1.06E-03	4.80	5.58E-04	4.79
	1/40	3674	3.43E-05	4.95	1.59E-05	5.13
	1/80	14860	9.68E-07	5.11	4.95E-07	4.97
	1/160	58330	3.33E-08	4.93	1.61E-08	5.01

Table 4: Accuracy order test for sixth order schemes

	$h$	$N_e$	$L^\infty$ error	$L^\infty$ order	$L^2$ error	$L^2$ order
Linear	1/13	374	7.94E-04	-	3.17E-04	-
	1/20	918	8.25E-05	5.04	2.60E-05	5.57
	1/40	3674	1.21E-06	6.08	3.50E-07	6.22
	1/80	14860	2.21E-08	5.73	5.48E-09	5.95
	1/160	58330	3.72E-10	5.97	9.69E-11	5.90
TEN06	1/13	374	7.94E-04	-	3.17E-04	-
	1/20	918	8.25E-05	5.04	2.60E-05	5.57
	1/40	3674	1.21E-06	6.08	3.50E-07	6.22
	1/80	14860	2.21E-08	5.73	5.48E-09	5.95
	1/160	58330	3.72E-10	5.97	9.69E-11	5.90

### 5.2. 2D solid body rotation problem

Next we consider the solid body rotation problem from Leveque [45]. The computational domain is  $[0, 1] \times [0, 1]$  with periodic boundary conditions applied for all directions. Three bodies are considered in this case, i.e. a

cosine function (SB01), a sharp cone (SB02) and a slotted cylinder (SB03). The functions, center locations and radius to describe the three bodies are provided in Table 5. The bodies are advected by an initial velocity  $\mathbf{v}(x, y) = (0.5 - y, x - 0.5)$  around the center of the domain, i.e.  $(x_c, y_c) = (0.5, 0.5)$ . At  $t = 2\pi$ , the analytical profile coincides with the initial solution. A uniform triangular mesh of edge length  $h = 1/80$  is used and the total number of mesh elements is 14860.

Table 5: Initial condition for the 2D solid body rotation problem

	$\mathbf{f}(x, y)$	center $(x_0, y_0)$	radius $r_0$
SB01	$\frac{1}{4}(1 + \cos(\pi r(x, y)))$	(0.25, 0.5)	0.15
SB02	$1 - (1/r_0)\sqrt{(x - x_0)^2 + (y - y_0)^2}$	(0.5, 0.25)	0.15
SB03	$\begin{cases} 1, & \text{if }  x - x_0  \geq 0.025 \text{ or } y \geq 0.85, \\ 0, & \text{otherwise.} \end{cases}$	(0.5, 0.75)	0.15

As shown in Fig. 2, the high-order TENO schemes, i.e. TENO4, TENO5 and TENO6, show much less numerical dissipation than the third-order TENO3 in capturing the slotted cylinder. Moreover, as demonstrated in Fig. 3, TENO5 generates less numerical overshoots than WENO5 and less dissipation than CWENO5 in preserving the shape of the cylinder.

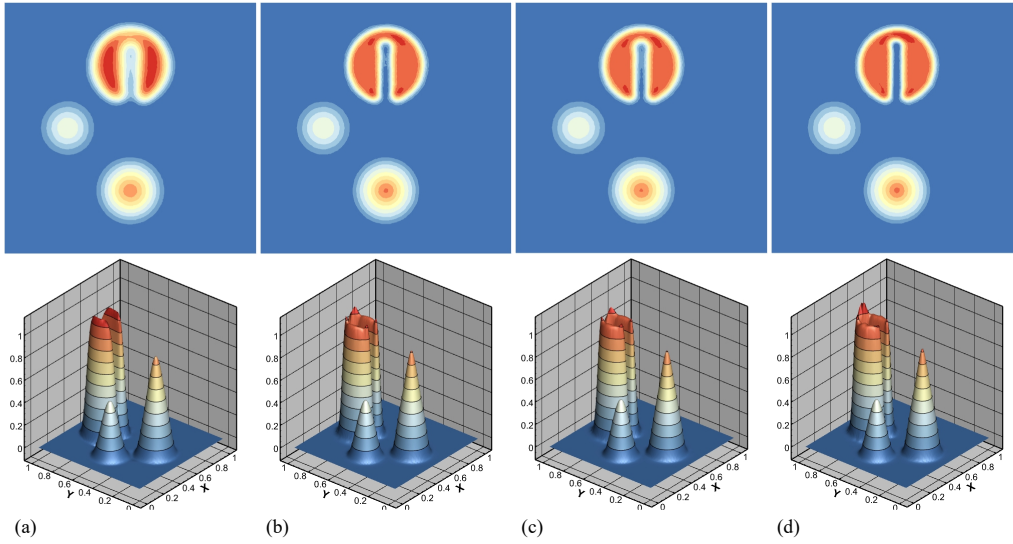


Figure 2: 2D solid body rotation problem: results from the (a) TENO3, (b) TENO4, (c) TENO5 and (d) TENO6 schemes after one rotation evolution at  $t = 2\pi$ . The uniform triangular mesh of edge length  $h = 1/80$  is used.

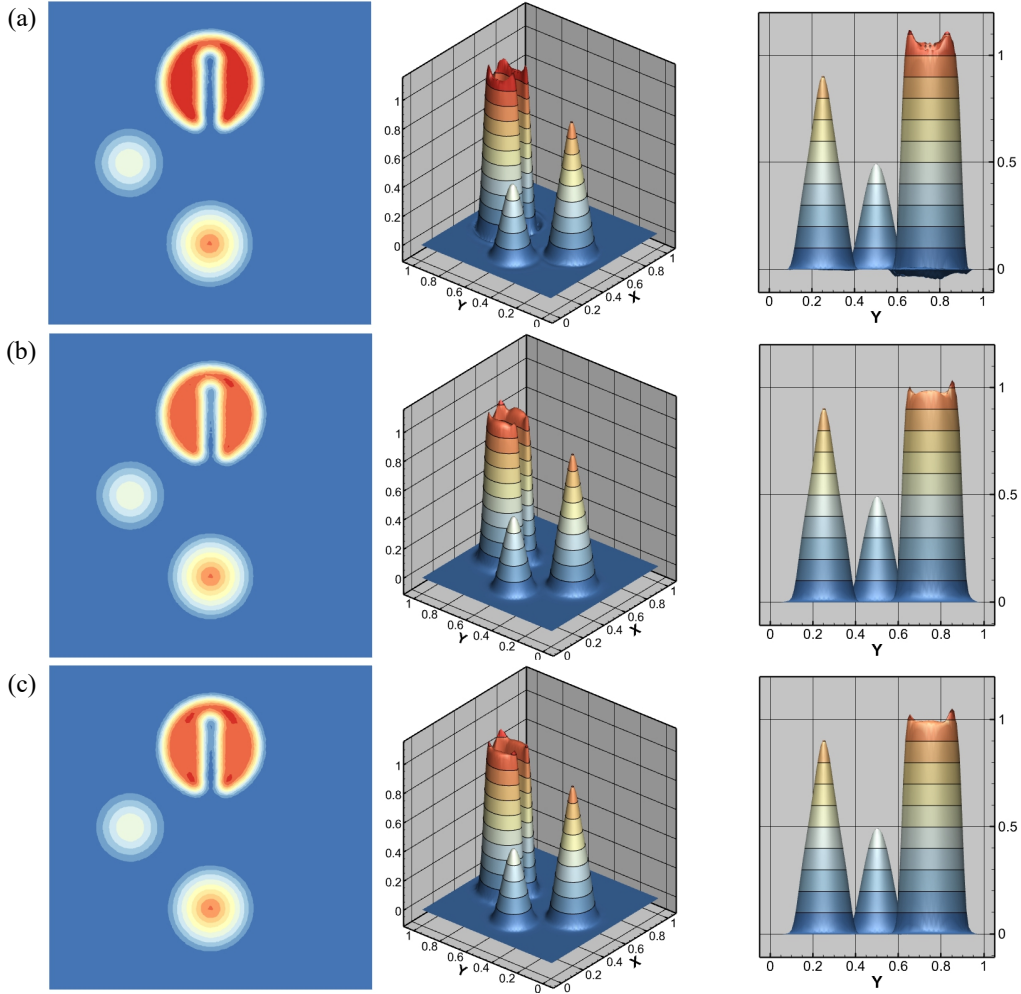


Figure 3: 2D solid body rotation problem: results from the (a) WENO5, (b) CWENO5 and (c) TENO5 schemes after one rotation evolution at  $t = 2\pi$ . The uniform triangular mesh of edge length  $h = 1/80$  is used.

### 5.3. 1D shock-tube problems

The initial state for the 1D shock tube (ST) problems [16] is

$$(\rho, u, p) = \begin{cases} (\rho_L, u_L, p_L), & \text{if } 0 \leq x < x_d, \\ (\rho_R, u_R, p_R), & \text{if } x_d \leq x \leq 1, \end{cases} \quad (39)$$

where  $L$  and  $R$  denotes the left and right states regarding to the location of discontinuity at  $x = x_d$ . The final simulation time is  $t = t_{end}$ . We consider

three variations of this problem, i.e. ST01/02/03, and all the parameters are given in Table 6. The computational domain is  $[0, 0.2] \times [0, 1]$ . For this case, the uniform Cartesian mesh is employed with an effective resolution of  $h = 1/100$  and the conservative variables are deployed for the high-order reconstruction due to the simplicity.

Table 6: Parameters of the 1D shock-tube problems.

	$\rho_L$	$u_L$	$p_L$	$\rho_R$	$u_R$	$p_R$	$t_{end}$	$x_d$
ST01 (Sod)	1.0	0.0	1.0	1.0	0.125	0.0	0.2	0.5
ST02 (Lax)	0.445	0.698	3.528	3.528	0.5	0.0	0.14	0.5
ST03	1.0	0.0	1000	1000	1.0	0.0	0.012	0.6

The computed density profiles are given in Fig. 4. Overall speaking, the discontinuities are captured without spurious oscillations by the TENO schemes of various orders. There are slight overshoots near the contact waves for the ST02 problem, which are also observed even for the results from other finite-difference low-dissipation schemes on structured meshes [26].

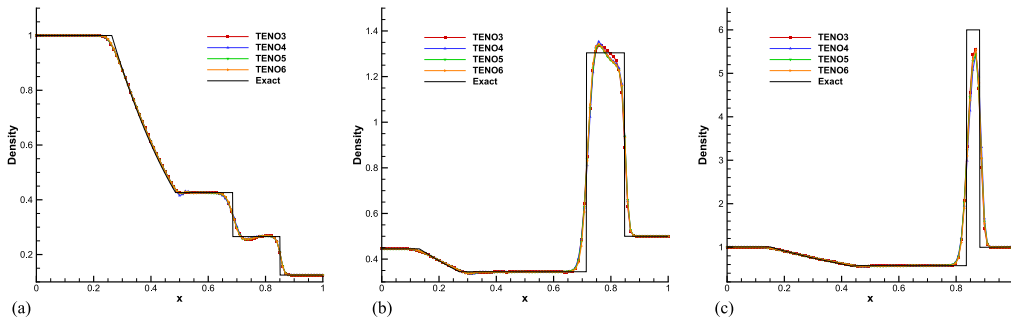


Figure 4: 1D shock-tube problems: results of (a) ST01, (b) ST02 and (c) ST03 with TENO schemes of different orders. The mesh resolution is  $h = 1/100$ .

#### 5.4. 1D shock-density wave interaction

The initial condition is given as [64]

$$(\rho, u, p) = \begin{cases} (3.857, 2.629, 10.333), & \text{if } 0 \leq x < 1, \\ (1 + 0.2 \sin(5(x - 5)), 0, 1), & \text{if } 1 \leq x \leq 10. \end{cases} \quad (40)$$

The computational domain is  $[0, 2] \times [0, 10]$  with 18, 282 uniformly distributed triangular mesh cells, i.e.  $h \approx 1/20$ , and the final evolution time is  $t =$

1.8. The “exact” solution is obtained by the 1D fifth-order finite-difference WENO5-JS scheme with 2000 cells.

As shown in Fig. 5, 6, and 7, with increasing accuracy order, the TENO schemes resolve the high-wavenumber fluctuations significantly better while maintaining the sharp shock-capturing capability. No artificial overshoots and oscillations are observed. In particular, the TENO5 and TENO6 schemes perform better than the CWENO schemes of the same accuracy order, suggesting less numerical dissipation.

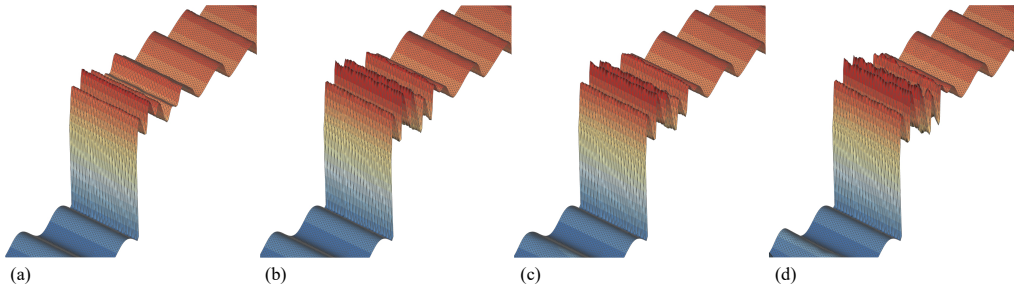


Figure 5: 1D shock-density wave interaction: density distributions from the (a) TENO3, (b) TENO4, (c) TENO5 and (d) TENO6 schemes. Also shown is the mesh topology on top of the density distributions. The uniformly distributed triangular mesh with  $h \approx 1/20$  is adopted.

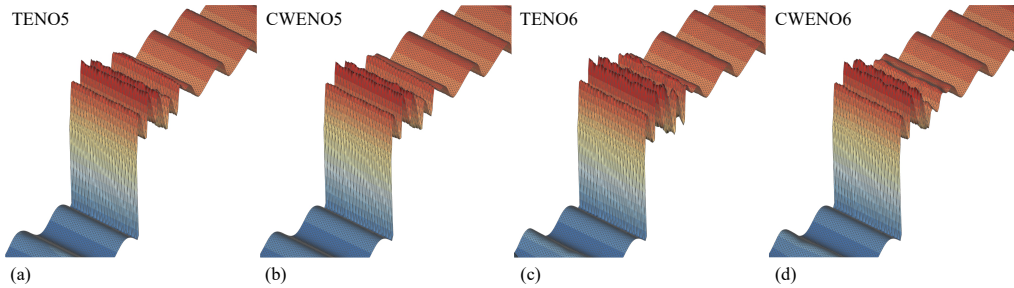


Figure 6: 1D shock-density wave interaction: density distributions from the (a) TENO5, (b) CWENO5, (c) TENO6 and (d) CWENO6 schemes. Also shown is the mesh topology on top of the density distributions. The uniformly distributed triangular mesh with  $h \approx 1/20$  is adopted.

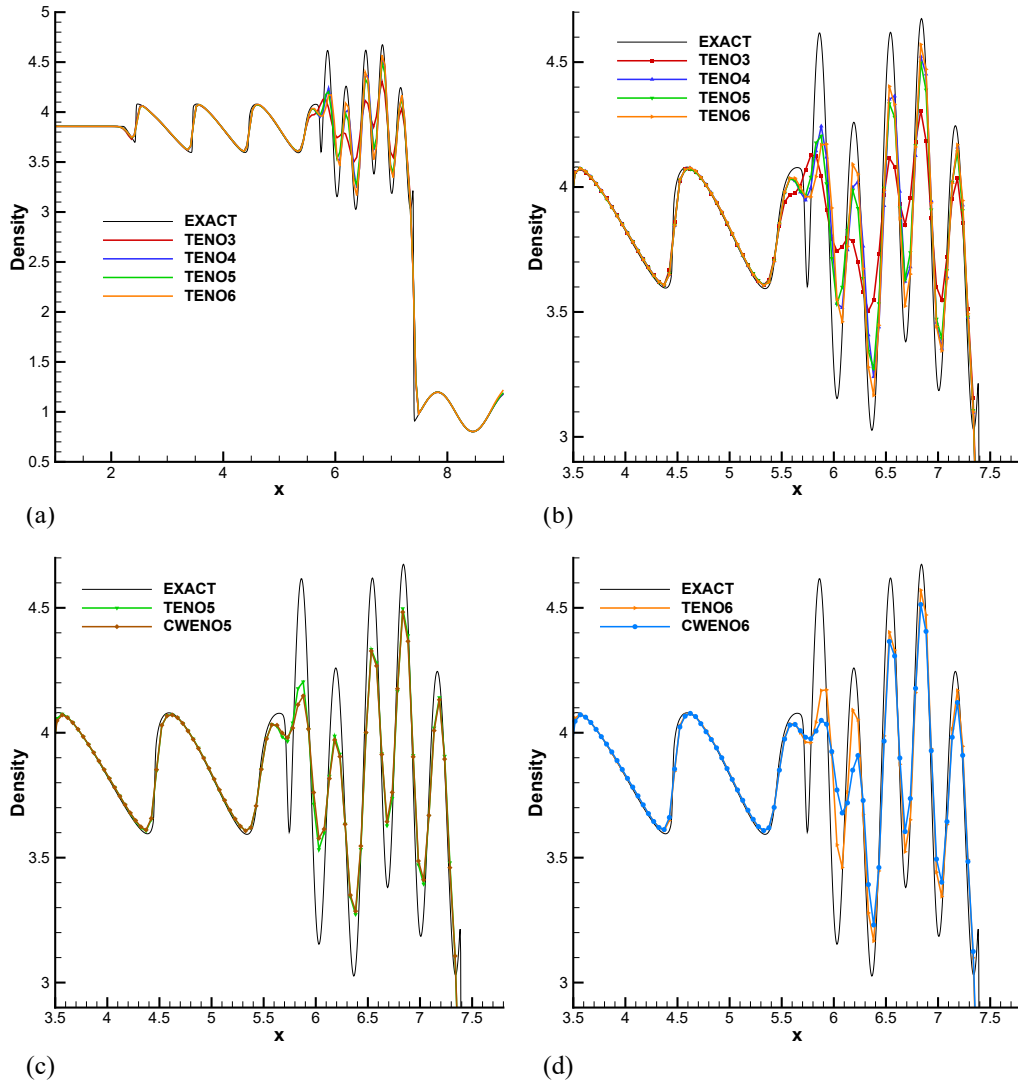


Figure 7: 1D shock-density wave interaction: (a) density and (b) zoomed-in view of density profiles from TENO schemes of different orders. Also included are the comparisons between (c) TENO5 and CWENO5, and (d) TENO6 and CWENO6 for density profiles. The uniformly distributed triangular mesh with  $h \approx 1/20$  is adopted.

### 5.5. 2D explosion problems

Two 2D explosion problems, referred as EP01 and EP02, are considered. The computational domain is given by a unit circle of radius  $R = 1$  centered at

[1, 1]. The computational domain is discretized by 18,464 triangular meshes, i.e. with an effective resolution of  $h \approx 1/50$ . The initial condition for problem EP01 is

$$(\rho, u, v, p)(\mathbf{r}, 0) = \begin{cases} (1.0, 0, 0, 1.0), & \text{if } \|\mathbf{r}\| \leq 0.5, \\ (0.125, 0, 0, 0.1), & \text{otherwise.} \end{cases} \quad (41)$$

The final simulation time is  $t = 0.2$ .

As shown in Fig. 8, 9, and 10, for both the density and pressure profiles of EP01, the present TENO schemes with various orders preserve the monotonicity pretty well as well as the corresponding WENO5 and CWENO5 schemes.

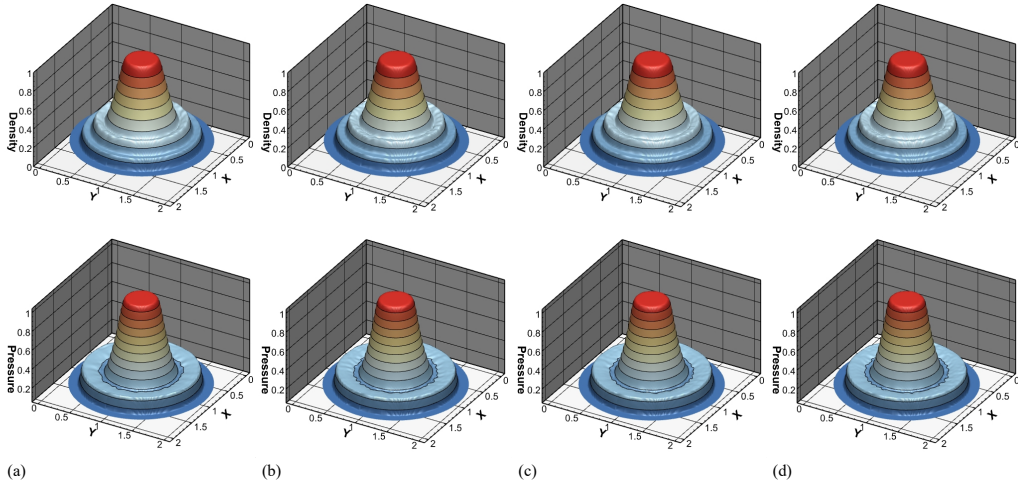


Figure 8: EP01: results from the (a) TENO3, (b) TENO4, (c) TENO5 and (d) TENO6 schemes. The upper row shows the density profiles and the bottom row shows the pressure profiles. A uniform triangular mesh with edge length  $h \approx 1/50$  is used.

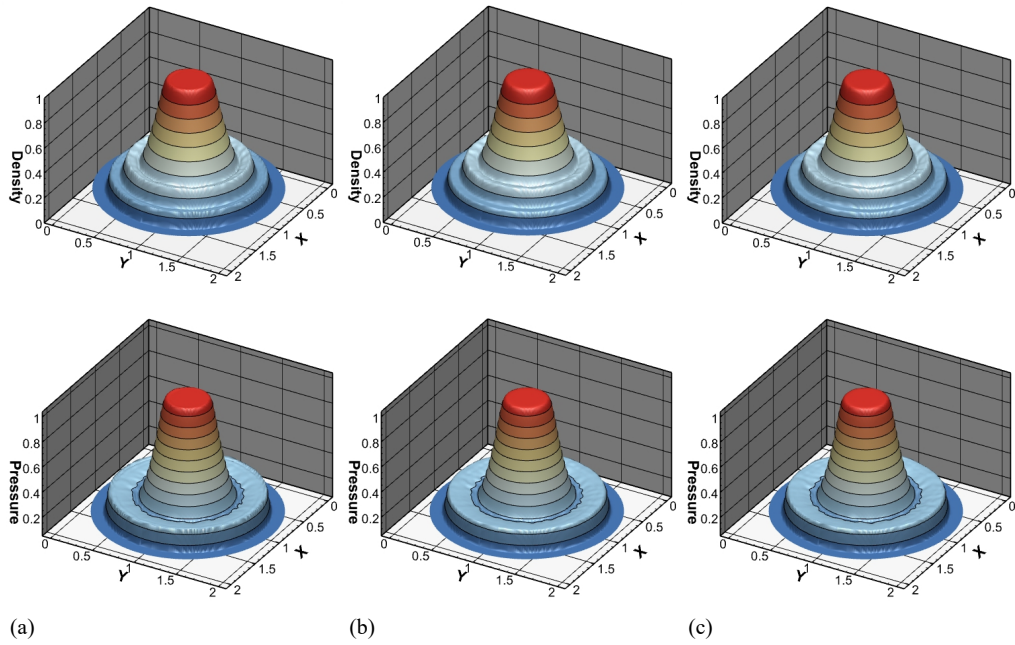


Figure 9: EP01: results from the (a) WENO5, (b) CWENO5 and (c) TENO5 schemes. The upper row shows the density profiles and the bottom row shows the pressure profiles. A uniform triangular mesh with edge length  $h \approx 1/50$  is used.

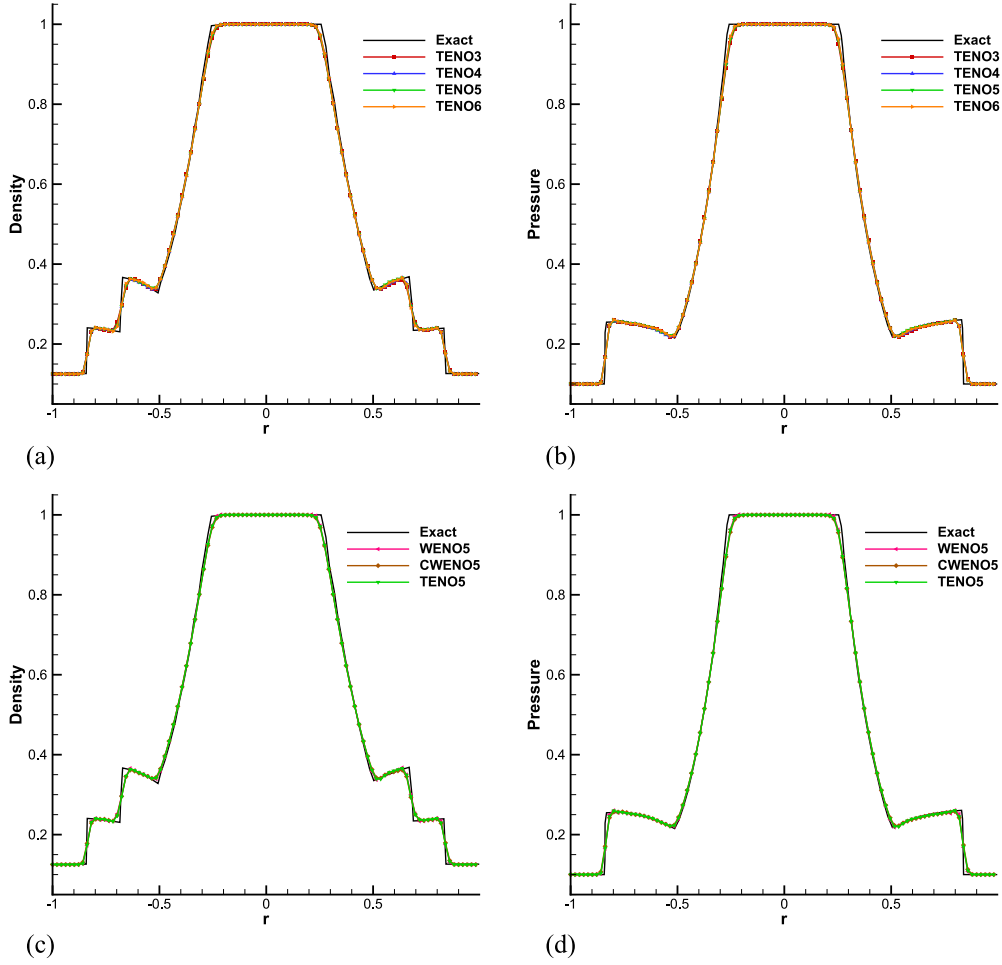


Figure 10: EP01: (a) density and (b) pressure profiles from TENO schemes of different orders. (c) density and (d) pressure profiles from the TENO5, WENO5 and CWENO5 schemes. A uniform triangular mesh with edge length  $h \approx 1/50$  is used.

The initial condition for problem EP02 is

$$(\rho, u, v, p)(\mathbf{r}, 0) = \begin{cases} (1.0, 0, 0, 2.0), & \text{if } \|\mathbf{r}\| \leq 0.5, \\ (1.0, 0, 0, 1.0), & \text{otherwise.} \end{cases} \quad (42)$$

The final simulation time is  $t = 0.2$ .

In terms of the EP02 problem, similar performance for resolving the density and pressure profiles is obtained for the various TENO schemes and the

CWENO5 scheme, as shown in Fig. 11, 12, and 13. However, the WENO5 scheme generates spurious numerical oscillations near the discontinuities, which can be observed from Fig. 12(a), Fig. 13(c), and Fig. 13(d).

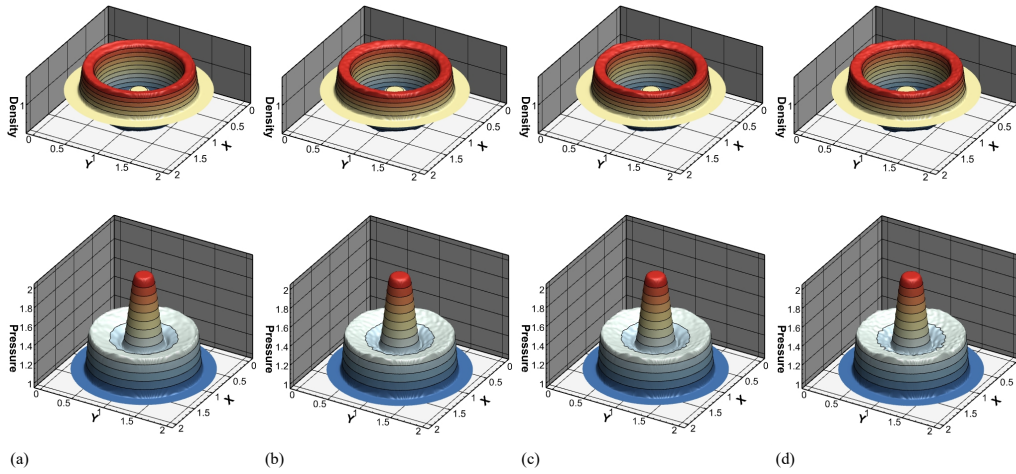


Figure 11: EP02: results from the (a) TENO3, (b) TENO4, (c) TENO5 and (d) TENO6 schemes. The upper row shows the density profiles and the bottom row shows the pressure profiles. A uniform triangular mesh with edge length  $h \approx 1/50$  is used.

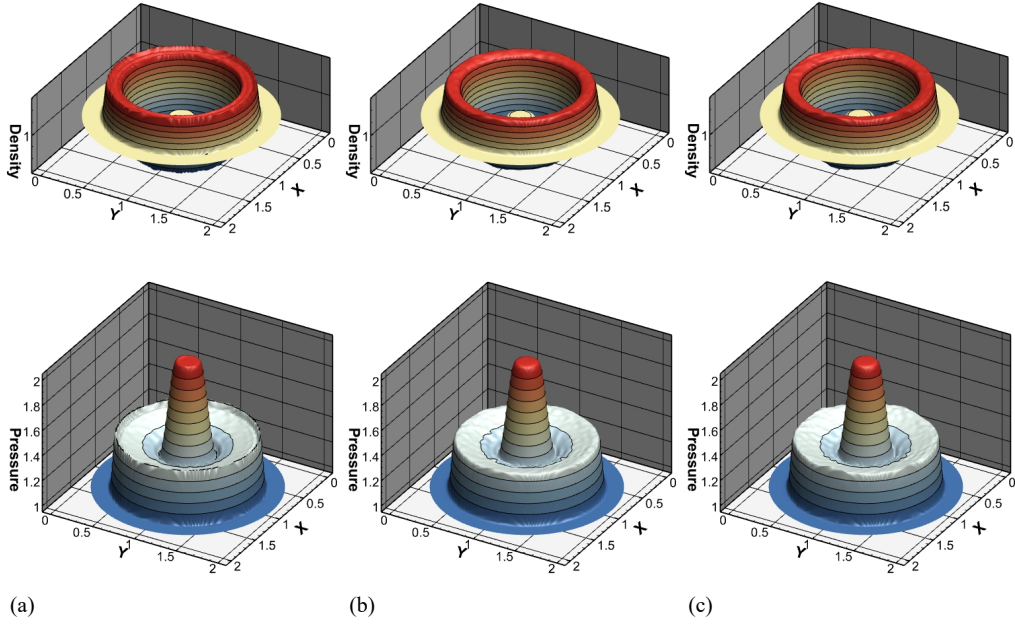


Figure 12: EP02: results from the (a) WENO5, (b) CWENO5 and (c) TENO5 schemes. The upper row shows the density profiles and the bottom row shows the pressure profiles. A uniform triangular mesh with edge length  $h \approx 1/50$  is used.

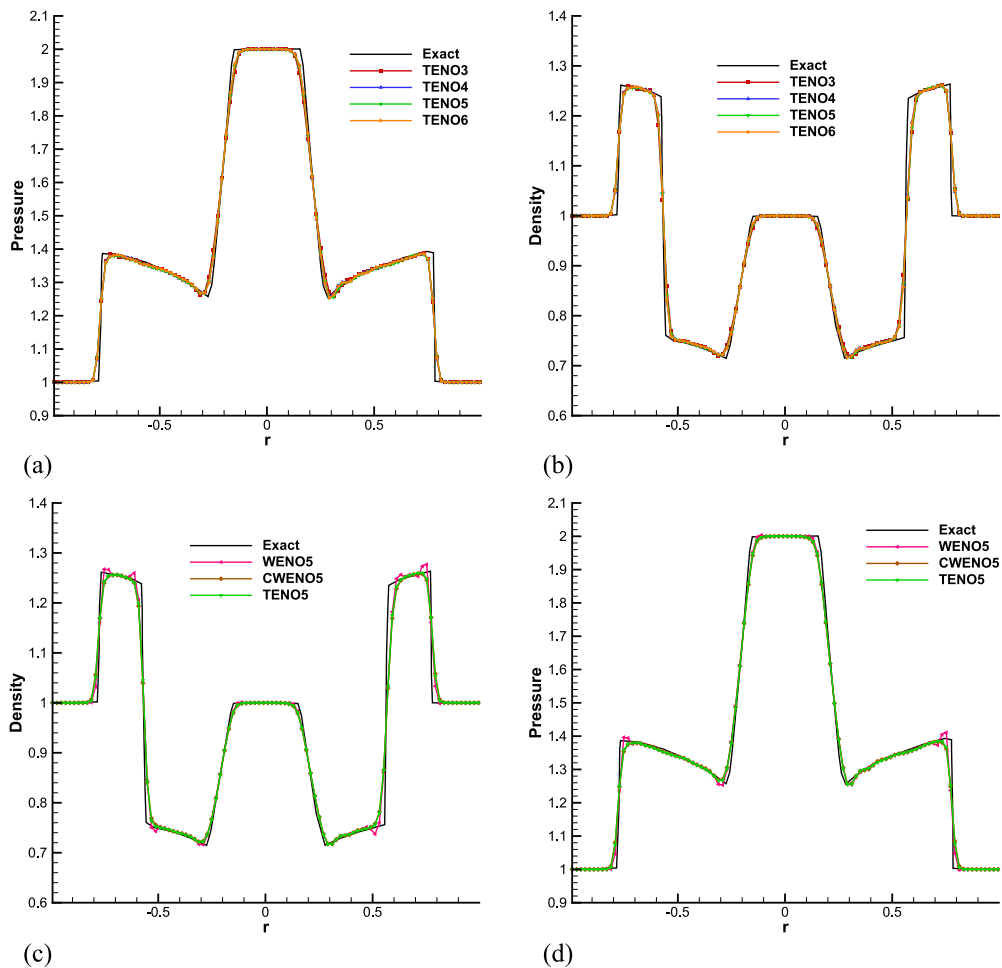


Figure 13: EP02: (a) density and (b) pressure profiles from TENO schemes of different orders; (c) density and (d) pressure profiles from the TENO5, WENO5 and CWENO5 schemes. A uniform triangular mesh with edge length  $h \approx 1/50$  is used.

### 5.6. 2D Kelvin-Helmholtz instability (KHI)

The Kelvin-Helmholtz instability with single mode perturbation is considered [59][58]. The computational domain is  $[-0.5, 0.5] \times [-0.5, 0.5]$  and the initial conditions are given as

$$(\rho, u) = \begin{cases} (2, -0.5), & |y| \leq 0.25, \\ (1, 0.5), & \text{otherwise,} \end{cases} \quad (43)$$

and

$$(v, p) = (0.01 \sin(2\pi x), 2.5). \quad (44)$$

$\gamma = 1.4$  and periodic boundary conditions are enforced at the boundaries of the computational domain. The final simulation time is  $t = 1$ .

The density distributions computed by various TENO, WENO and CWENO schemes are given by Fig. 14, 15, and 16. The third-order TENO3 scheme is much more dissipative than other TENO schemes of higher order and smears the small-scale vortical structures significantly. As shown in Fig. 16, the TENO5 and TENO6 schemes perform much better than the CWENO5 and CWENO6 schemes in terms of preserving the kinetic energy.

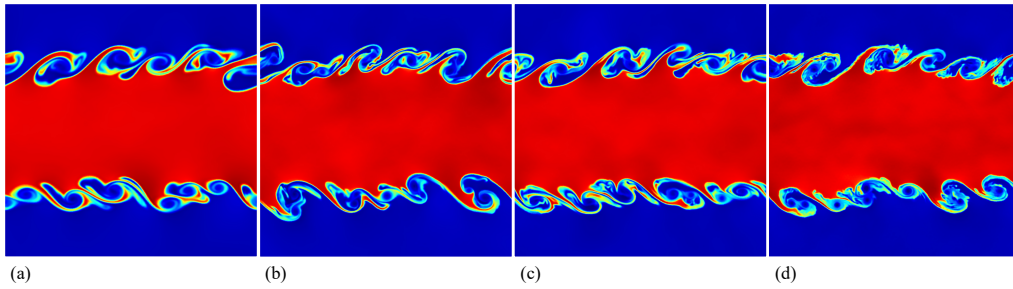


Figure 14: 2D Kelvin-Helmholtz instability: density distributions at  $t = 1$  from the (a) TENO3, (b) TENO4, (c) TENO5 and (d) TENO6 schemes. The uniformly distributed triangular mesh with an effective resolution  $h \approx 1/500$  is adopted.

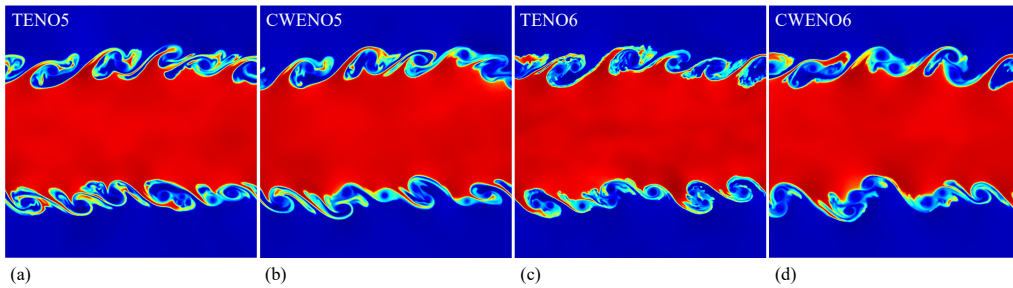


Figure 15: 2D Kelvin-Helmholtz instability: density distributions at  $t = 1$  from the (a) TENO5, (b) CWENO5, (c) TENO6 and (d) CWENO6 schemes. The uniformly distributed triangular mesh with an effective resolution  $h \approx 1/500$  is adopted.

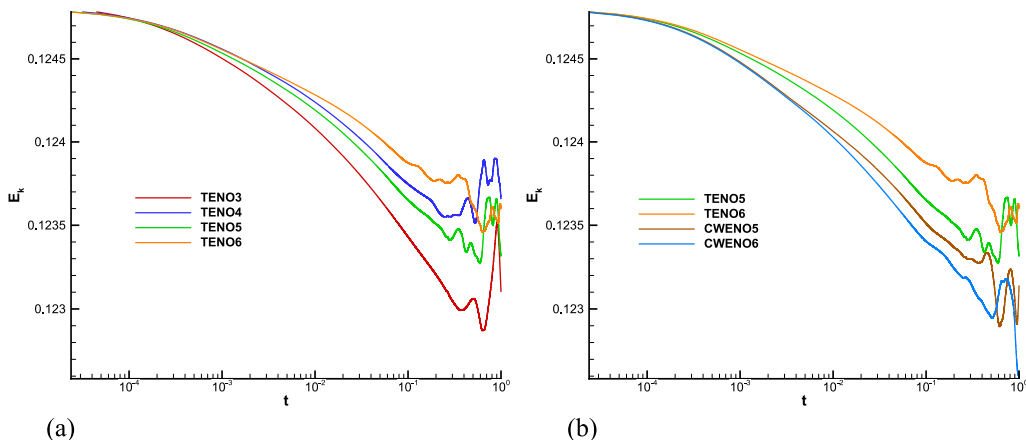


Figure 16: 2D Kelvin-Helmholtz instability: density profiles from (a) TENO schemes of different orders and comparisons between (b) TENO5/6 and CWENO5/6. The uniformly distributed triangular mesh with an effective resolution  $h \approx 1/500$  is adopted.

### 5.7. 2D double Mach reflection of a strong shock (DMR)

The initial condition is [80]

$$(\rho, u, v, p) = \begin{cases} (1.4, 0, 0, 1), & \text{if } y < 1.732(x - 0.1667), \\ (8, 7.145, -4.125, 116.8333), & \text{otherwise.} \end{cases} \quad (45)$$

The computational domain is  $[0, 4] \times [0, 1]$  and the simulation end time is  $t = 0.2$ . Initially, a right-moving Mach 10 shock wave is placed at  $x = 0.1667$  with an incident angle of  $60^\circ$  to the x-axis. The post-shock condition is imposed from  $x = 0$  to  $x = 0.1667$  whereas a reflecting wall condition is enforced from  $x = 0.1667$  to  $x = 4$  at the bottom. For the top boundary condition, the fluid variables are defined to exactly describe the evolution of the Mach 10 shock wave. The inflow and outflow condition are imposed for the left and right sides of the computational domain.

The numerical results from TENO schemes of various orders and the corresponding CWENO and WENO schemes are given in Fig. 17, 18, 19, 20, 21, 22, and 23. As shown in Fig. 17, 18 and 19, with the same mesh resolution, the TENO schemes with higher-order resolve the small-scale features much better with less numerical dissipation. The zoomed-in view of the density distributions in Fig. 20 shows that no spurious numerical oscillations present in the

vicinity of the discontinuities. As given by Fig. 21, 22 and 23, when compared with the WENO and CWENO schemes of same orders, the TENO schemes feature the least numerical dissipation, followed by the WENO schemes and subsequently by the CWENO schemes. It is worth noting that, while both the TENO and CWENO schemes are robust for all the considered mesh resolutions, the WENO5 and WENO6 schemes typically fail the simulations without an additional limiter [69], which helps preserve the positivity of density and pressure.

Moreover, when compared to the newly proposed fifth-order WENO5-AO scheme, the present TENO5 scheme performs better in capturing the roll-up of the Mach stem with half resolution in each coordinate direction, see their Fig. 4 of [2]. The result from the present TENO5 scheme at the resolution of  $h \approx 1/200$  is comparable to that from the multi-resolution WENO5 scheme at the the resolution of  $h \approx 1/320$  in [87].

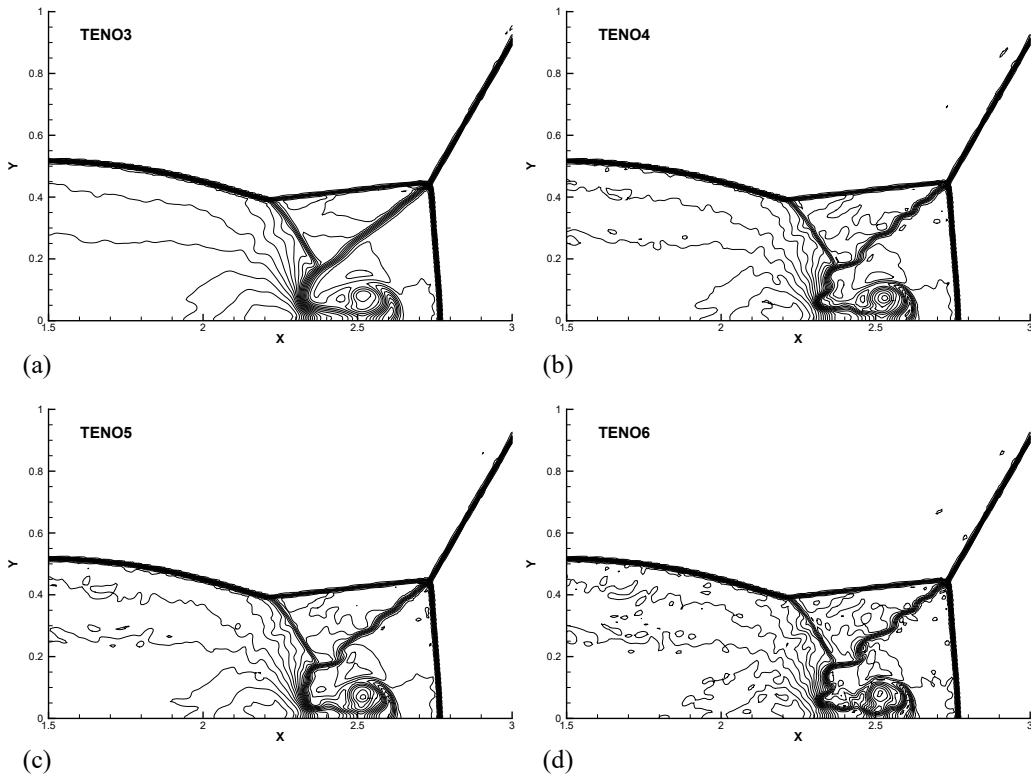


Figure 17: 2D double Mach reflection of a strong shock: results from the (a) TENO3, (b) TENO4, (c) TENO5 and (d) TENO6 schemes. The figures are drawn with 43 density contours between 1.887 and 20.9. The mesh has 151,850 uniform triangular elements and  $h \approx 1/125$ .

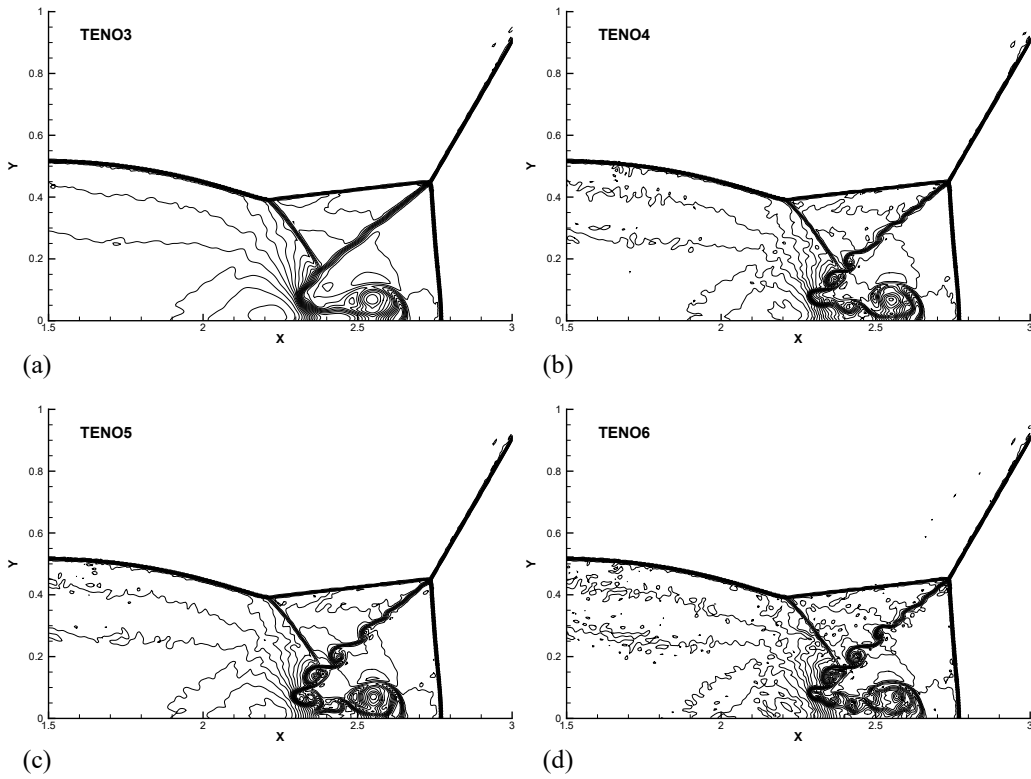


Figure 18: 2D double Mach reflection of a strong shock: results from the (a) TENO3, (b) TENO4, (c) TENO5 and (d) TENO6 schemes. The figures are drawn with 43 density contours between 1.887 and 20.9. The mesh has 369,794 uniform triangular elements and  $h \approx 1/200$ .

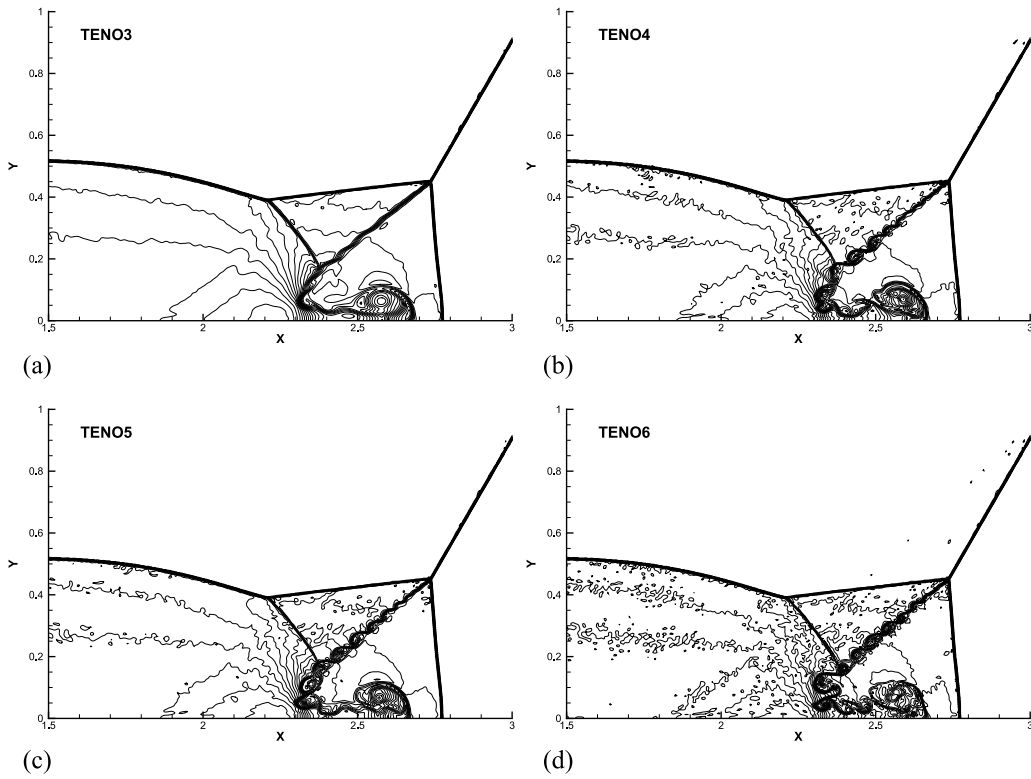


Figure 19: 2D double Mach reflection of a strong shock: results from the (a) TENO3, (b) TENO4, (c) TENO5 and (d) TENO6 schemes. The figures are drawn with 43 density contours between 1.887 and 20.9. The mesh has 752,708 uniform triangular elements and  $h \approx 1/280$ .

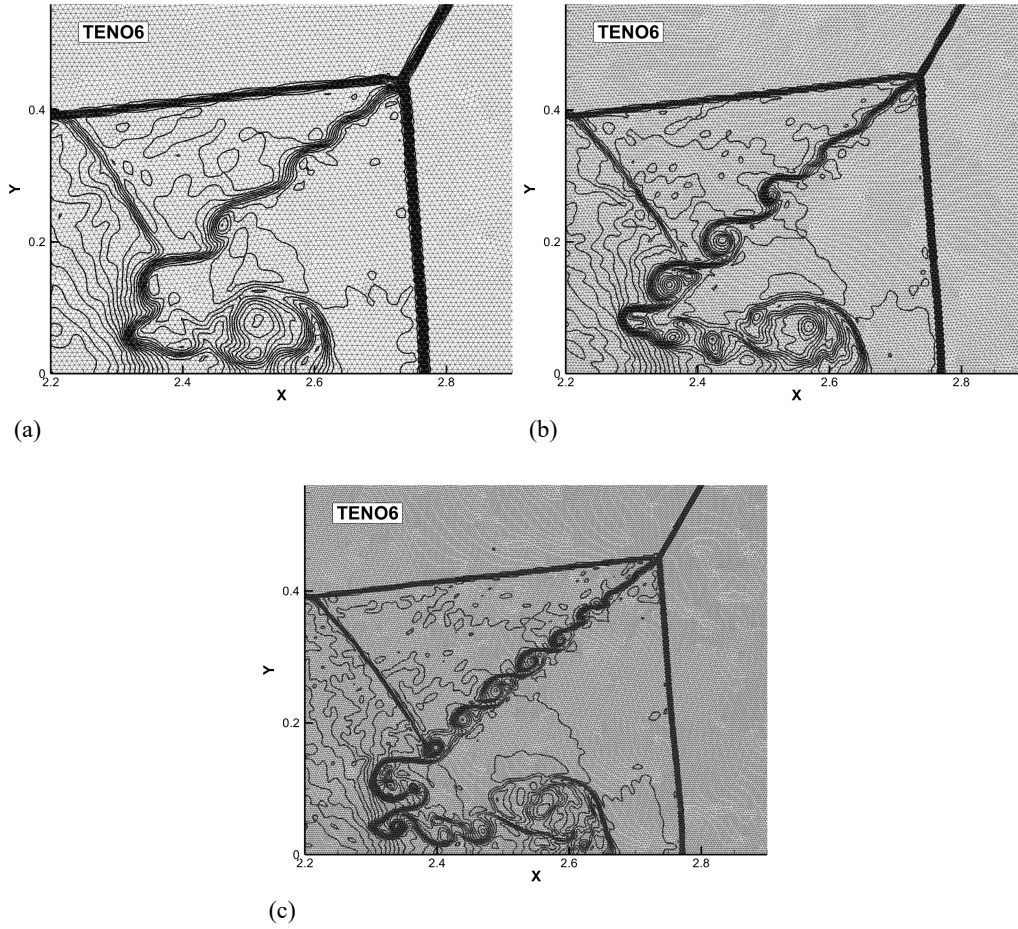


Figure 20: 2D double Mach reflection of a strong shock: zoomed-in results from the TENO6 scheme with (a) 151,850, (b) 369,794 and (c) 752,708 uniform triangular elements. The figures are drawn with 43 density contours between 1.887 and 20.9. Also plotted are the mesh typologies.

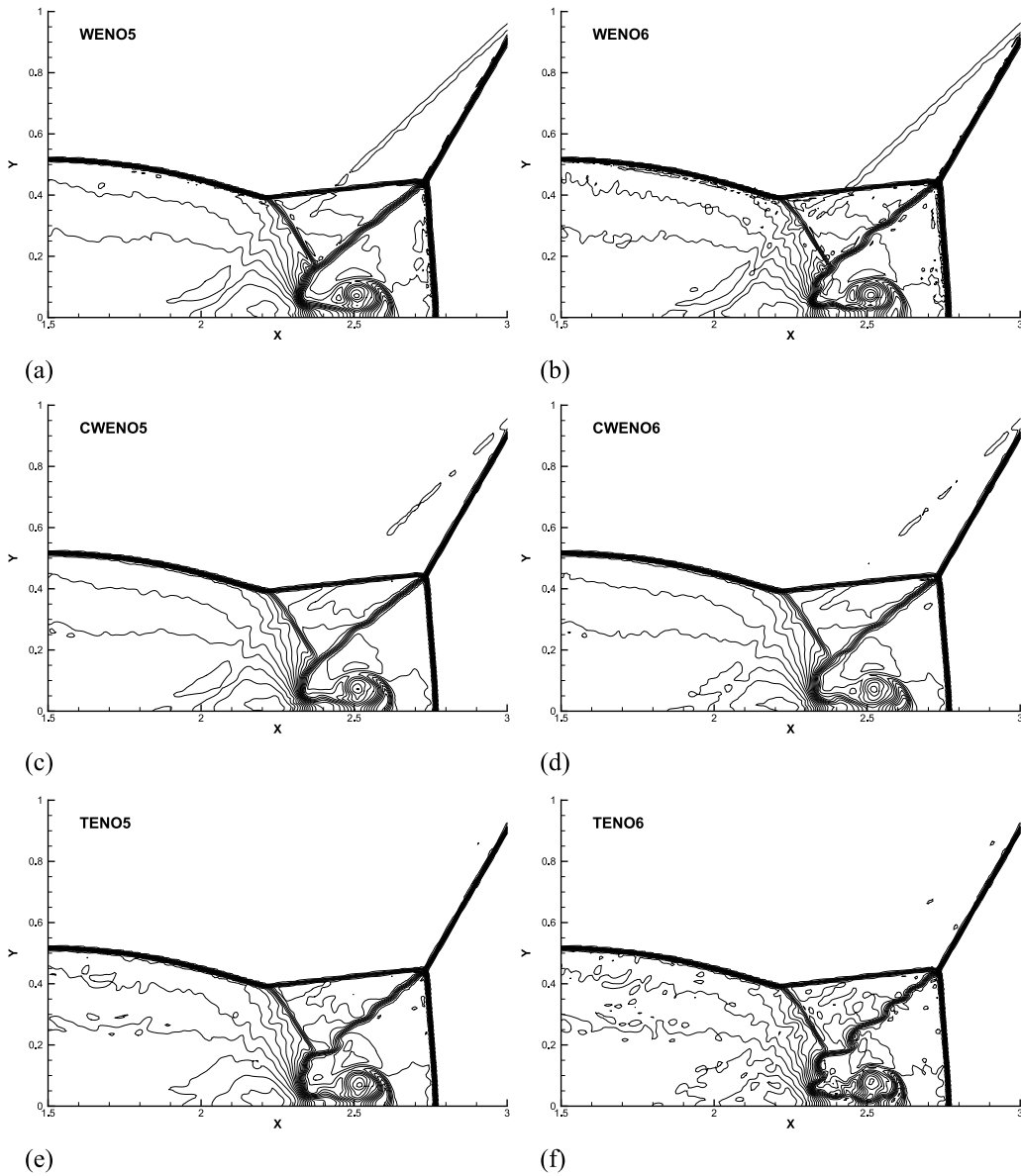


Figure 21: 2D double Mach reflection of a strong shock: results from the (a) WENO5, (b) WENO6, (c) CWENO5, (d) CWENO6, (e) TENO5, (f) TENO6 schemes. The figures are drawn with 43 density contours between 1.887 and 20.9. The mesh has 151,850 uniform triangular elements and  $h \approx 1/125$ . Note that the WENO6 scheme fails at this resolution without the additional limiter in [69].

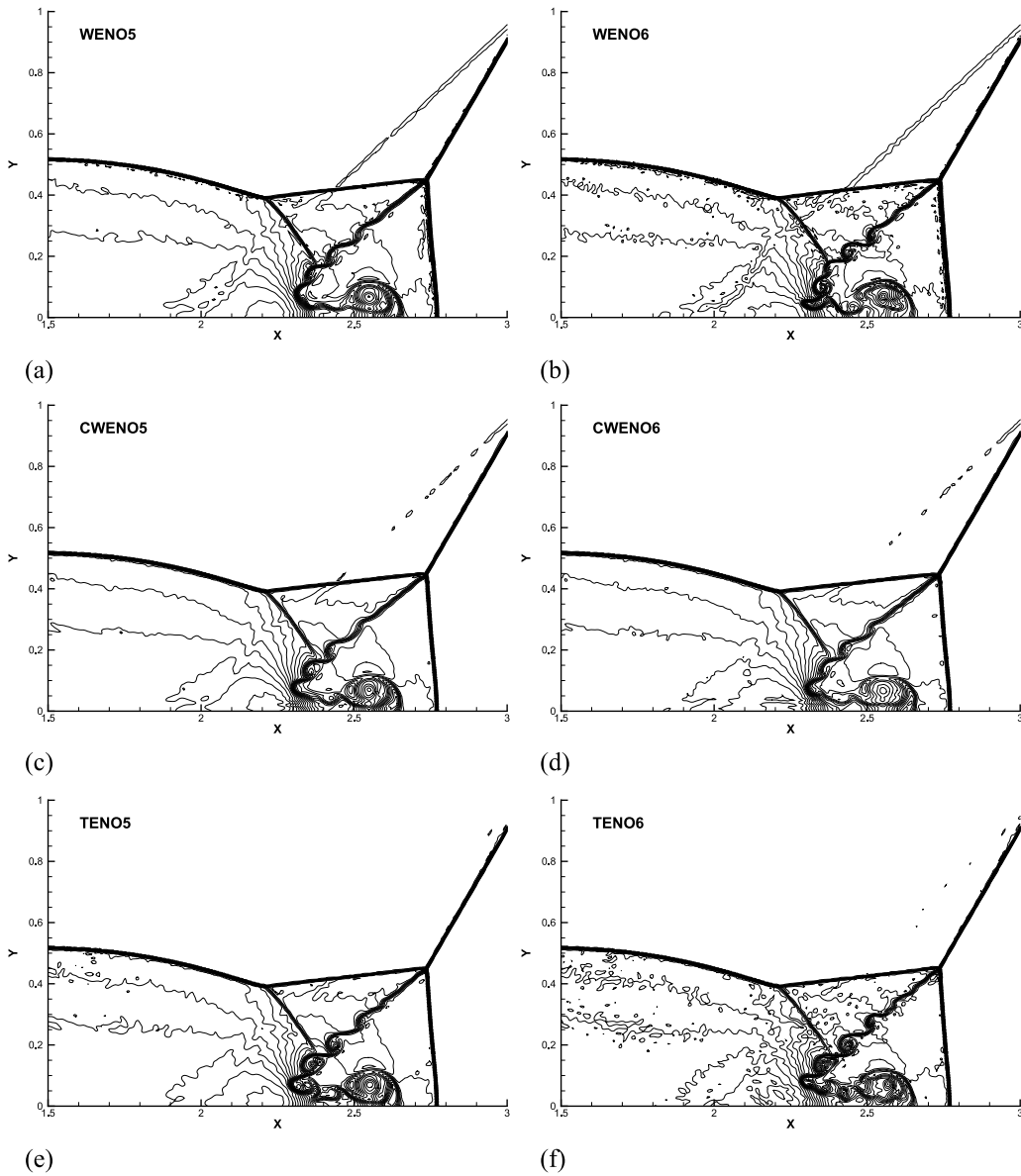


Figure 22: 2D double Mach reflection of a strong shock: results from the (a) WENO5, (b) WENO6, (c) CWENO5, (d) CWENO6, (e) TENO5, (f) TENO6 schemes. The figures are drawn with 43 density contours between 1.887 and 20.9. The mesh has 369,794 uniform triangular elements and  $h \approx 1/200$ . Note that both the WENO5 and WENO6 schemes fail at this resolution without the additional limiter in [69].

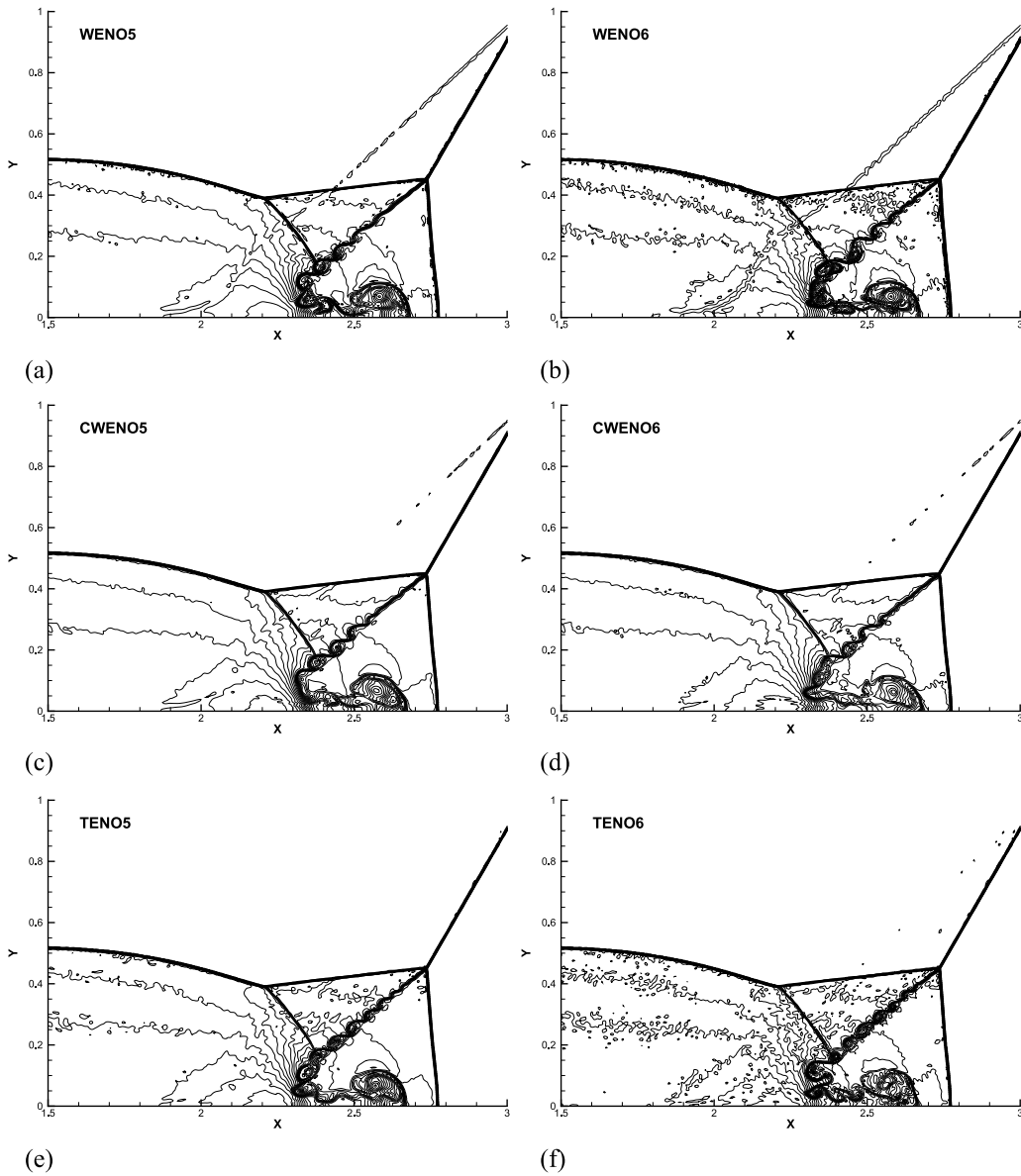


Figure 23: 2D double Mach reflection of a strong shock: results from the (a) WENO5, (b) WENO6, (c) CWENO5, (d) CWENO6, (e) TENO5, (f) TENO6 schemes. The figures are drawn with 43 density contours between 1.887 and 20.9. The mesh has 752,708 uniform triangular elements and  $h \approx 1/280$ . Note that the WENO6 scheme fails at this resolution without the additional limiter in [69].

### 5.8. Efficiency analysis

Table 7 lists the statistics regarding the computing time of different schemes, where  $N_{iter}$  denotes the number of iterations to complete the calculation,  $t_{total}$  the total computing time in seconds and  $t_{recon}$  the computing time for the high-order reconstruction. Upon further normalization by  $N_{iter}$  and  $N_e$ , we obtain  $t_{norm}$  (second/iteration/element) from  $t_{recon}$ . Two cases are considered for the analysis, i.e. the 2D DMR and the 2D KHI. The total number of mesh elements is 369,794 and 577,416, respectively. For DMR, we measure the total computing time at  $t = 2$  and for KHI, the total computing time is measured at  $t = 0.1$ .

By increasing the accuracy order of TENO schemes from third- to sixth-order, the normalized cost increases by roughly 65% for the same simulation. Overall speaking, the TENO and CWENO schemes with the same accuracy order feature a similar computational efficiency for both cases.

Table 7: Computing-time statistics for TENO and CWENO schemes

	scheme	$N_{iter}$	$t_{total}$	$t_{recon}$	$t_{norm}$
DMR	TENO3	16007	9468.00	8079.77	1.36E-06
	TENO4	16110	12194.47	9895.88	1.66E-06
	TENO5	16081	13990.78	11674.00	1.96E-06
	TENO6	16152	16262.73	13358.49	2.24E-06
	CWENO5	16045	14126.61	11738.53	1.98E-06
	CWENO6	16019	15472.95	13016.93	2.20E-06
KHI	TENO3	3580	3298.40	2733.38	1.32E-06
	TENO4	3580	4201.04	3425.22	1.66E-06
	TENO5	3579	4587.06	3935.91	1.90E-06
	TENO6	3579	5399.16	4540.90	2.20E-06
	CWENO5	3578	4626.61	3887.51	1.88E-06
	CWENO6	3579	5414.79	4491.87	2.17E-06

\* Regarding the hardware configurations, the CPU used for the tests is Intel Xeon E5-2690. The Intel Fortran Compiler version 19 and the Intel MPI Library 2019 are employed for the compiling with the compiler flags `-i4 -r8 -ipo -march=core-avx2 -mtune=core-avx2 -O3 -fp-model precise -zero -qopenmp -qopenmp-link=static`. For both the DMR and KHI simulations, 56 parallel threads are employed, i.e. 8 MPI tasks with 7 OpenMP threads per MPI rank.

## 6. Conclusions

In this paper, the high-order TENO scheme, originally proposed for structured meshes, is for the first time extended to unstructured meshes. A set

of TENO schemes from third- to sixth-order accuracy is developed and validated. The concluding remarks are given as follows.

- The new candidate stencils include one large central-biased stencil and several small directional stencils. The targeted high-order reconstruction scheme is constructed on the large stencil while the third-order schemes are constructed on the small stencils. To achieve the same accuracy order in smooth regions, the present stencil arrangement leads to narrower full stencil width when compared to those deployed in [73][66][17][18].
- Following a strong scale separation procedure, a novel ENO-like stencil selection strategy is tailored for unstructured meshes. Such a TENO weighting strategy ensures that the high-order accuracy is restored by adopting the candidate reconstruction from the large stencil and the sharp shock-capturing capability is retained by selecting the candidate reconstruction from the smooth small stencils. As analyzed in previous work [26][28][23], one dissipation source of WENO family schemes comes from the smooth weighting of the contributions from candidate stencils, which leads to the early triggering of the nonlinear adaptations in the low-wavenumber regimes. Similar to those TENO schemes for Cartesian meshes, the low-dissipation property is inherited in the proposed schemes due to the sharp stencil selection, which either applies the candidate stencil in an optimal way or abandons it completely when crossed by genuine discontinuities.
- The new framework allows for arbitrarily high-order TENO reconstructions. For conceptual investigations, the TENO schemes from third- to sixth-order accuracy are constructed and the built-in parameters are explicitly given.
- A set of challenging benchmark simulations has been conducted with the default set of parameters. Numerical results reveal that the proposed TENO schemes are robust for highly compressible gas dynamic simulations with low numerical dissipation and sharp discontinuity-capturing capability.

- Compared to the WENO schemes with equal-size candidate stencils, the overall stencil width of the present TENO schemes is much more compact. Compared to the CWENO schemes with the same accuracy order, the proposed TENO schemes are much less dissipative while featuring the sharp shock-capturing capability. Note that, the present investigation also reveals that the WENO schemes with equal-size candidate stencils are less robust when deployed to strong discontinuities (as shown in the DMR simulations), which denotes another flaw in addition to the complex reconstruction procedure.

Considering the good performance of the proposed TENO framework and the flexibility for further extension, the future work will focus on the deployment of the present schemes to more complicated flows, e.g. the chemical reacting flows, the MHD flows, and the external aerodynamics with realistic geometries.

### **Declaration of Competing Interest**

The authors declare that they have no known competing financial interests or personal relationships that could have appeared to influence the work reported in this paper.

### **Acknowledgements**

Lin Fu acknowledges the generous startup fund from The Hong Kong University of Science and Technology (NO. R9280).

### **References**

- [1] Abbassi, H., Mashayek, F., Jacobs, G.B., 2014. Shock capturing with entropy-based artificial viscosity for staggered grid discontinuous spectral element method. *Computers & Fluids* 98, 152–163.
- [2] Balsara, D.S., Garain, S., Florinski, V., Boscheri, W., 2020. An efficient class of WENO schemes with adaptive order for unstructured meshes. *Journal of Computational Physics* 404, 109062.

- [3] Balsara, D.S., Garain, S., Shu, C.W., 2016. An efficient class of WENO schemes with adaptive order. *Journal of Computational Physics* 326, 780–804.
- [4] Barth, T., Jespersen, D., 1989. The design and application of upwind schemes on unstructured meshes, in: *27th Aerospace sciences meeting*, p. 366.
- [5] Batten, P., Clarke, N., Lambert, C., Causon, D., 1997. On the choice of wavespeeds for the HLLC Riemann solver. *SIAM Journal on Scientific Computing* 18, 1553–1570.
- [6] Borges, R., Carmona, M., Costa, B., Don, W.S., 2008. An improved weighted essentially non-oscillatory scheme for hyperbolic conservation laws. *Journal of Computational Physics* 227, 3191–3211.
- [7] Capdeville, G., 2008. A central WENO scheme for solving hyperbolic conservation laws on non-uniform meshes. *Journal of Computational Physics* 227, 2977–3014.
- [8] Cheng, J., Shu, C.W., 2008. A third order conservative Lagrangian type scheme on curvilinear meshes for the compressible Euler equations 4, 1008–1024.
- [9] Cockburn, B., Lin, S.Y., Shu, C.W., 1989. TVB Runge-Kutta local projection discontinuous Galerkin finite element method for conservation laws III: one-dimensional systems. *Journal of Computational Physics* 84, 90–113.
- [10] Cockburn, B., Shu, C.W., 1998. The Runge-Kutta discontinuous Galerkin method for conservation laws V: multidimensional systems. *Journal of Computational Physics* 141, 199–224.
- [11] Collis, S.S., 2002. Discontinuous Galerkin methods for turbulence simulation, in: *Proceedings of the Summer Program*, p. 155.
- [12] Cravero, I., Puppo, G., Semplice, M., Visconti, G., 2018. CWENO: uniformly accurate reconstructions for balance laws. *Mathematics of Computation* 87, 1689–1719.

- [13] Di Renzo, M., Fu, L., Urzay, J., 2020. HTR solver: An open-source exascale-oriented task-based multi-GPU high-order code for hypersonic aerothermodynamics. *Computer Physics Communications* 255, 107262.
- [14] Diskin, B., Thomas, J.L., 2007. Accuracy analysis for mixed-element finite-volume discretization schemes. NIA report 8.
- [15] Dong, H., Fu, L., Zhang, F., Liu, Y., Liu, J., 2019. Detonation simulations with a fifth-order TENO scheme. *Communications in Computational Physics* 25, 1357–1393.
- [16] Dumbser, M., Boscheri, W., Semplice, M., Russo, G., 2017. Central weighted ENO schemes for hyperbolic conservation laws on fixed and moving unstructured meshes. *SIAM Journal on Scientific Computing* 39, A2564–A2591.
- [17] Dumbser, M., Käser, M., 2007. Arbitrary high order non-oscillatory finite volume schemes on unstructured meshes for linear hyperbolic systems. *Journal of Computational Physics* 221, 693–723.
- [18] Dumbser, M., Käser, M., Titarev, V.A., Toro, E.F., 2007. Quadrature-free non-oscillatory finite volume schemes on unstructured meshes for nonlinear hyperbolic systems. *Journal of Computational Physics* 226, 204–243.
- [19] Einfeldt, B., Munz, C.D., Roe, P.L., Sjögren, B., 1991. On Godunov-type methods near low densities. *Journal of computational physics* 92, 273–295.
- [20] Fardipour, K., Mansour, K., 2020. Development of targeted compact nonlinear scheme with increasingly high order of accuracy. *Progress in Computational Fluid Dynamics, an International Journal* 20, 1–19.
- [21] Flad, D., Gassner, G., 2017. On the use of kinetic energy preserving DG-schemes for large eddy simulation. *Journal of Computational Physics* 350, 782–795.

- [22] Frère, A., Carton de Wiart, C., Hillewaert, K., Chatelain, P., Winckelmans, G., 2017. Application of wall-models to discontinuous Galerkin LES. *Physics of Fluids* 29, 085111.
- [23] Fu, L., 2019a. A low-dissipation finite-volume method based on a new TENO shock-capturing scheme. *Computer Physics Communications* 235, 25–39.
- [24] Fu, L., 2019b. A very-high-order TENO scheme for all-speed gas dynamics and turbulence. *Computer Physics Communications* 244, 117–131.
- [25] Fu, L., Hu, X.Y., Adams, N.A., . A FAMILY OF HIGH ORDER TARGETED ENO SCHEME FOR COMPRESSIBLE FLUID SIMULATIONS, in: Ninth International Symposium on Turbulence and Shear Flow Phenomena (TSFP-9), June 30 - July 3, 2015, The University of Melbourne, Australia, Begel House Inc.
- [26] Fu, L., Hu, X.Y., Adams, N.A., 2016. A family of high-order targeted ENO schemes for compressible-fluid simulations. *Journal of Computational Physics* 305, 333–359.
- [27] Fu, L., Hu, X.Y., Adams, N.A., 2017. Targeted ENO schemes with tailored resolution property for hyperbolic conservation laws. *Journal of Computational Physics* 349, 97–121.
- [28] Fu, L., Hu, X.Y., Adams, N.A., 2018. A new class of adaptive high-order targeted ENO schemes for hyperbolic conservation laws. *Journal of Computational Physics* 374, 724–751.
- [29] Fu, L., Hu, X.Y., Adams, N.A., 2019a. A Targeted ENO Scheme as Implicit Model for Turbulent and Genuine Subgrid Scales. *Communications in Computational Physics* 26, 311–345.
- [30] Fu, L., Hu, X.Y., Adams, N.A., 2019b. Improved Five- and Six-Point Targeted Essentially Nonoscillatory Schemes with Adaptive Dissipation. *AIAA Journal* 57, 1143–1158.

- [31] Fu, L., Karp, M., Bose, S.T., Moin, P., Urzay, J., 2021. Shock-induced heating and transition to turbulence in a hypersonic boundary layer. *Journal of Fluid Mechanics* 909, A8.
- [32] Fu, L., Tang, Q., 2019. High-order low-dissipation targeted ENO schemes for ideal magnetohydrodynamics. *Journal of Scientific Computing* 80, 692–716.
- [33] Gempesaw, D., 2011. A multi-resolution discontinuous Galerkin method for rapid simulation of thermal systems. Ph.D. thesis. Georgia Institute of Technology.
- [34] Gottlieb, S., Shu, C.W., Tadmor, E., 2001. Strong stability-preserving high-order time discretization methods. *SIAM review* 43, 89–112.
- [35] Haga, T., Kawai, S., 2019. On a robust and accurate localized artificial diffusivity scheme for the high-order flux-reconstruction method. *Journal of Computational Physics* 376, 534–563.
- [36] Haimovich, O., Frankel, S.H., 2017. Numerical simulations of compressible multicomponent and multiphase flow using a high-order targeted ENO (TENNO) finite-volume method. *Computers & Fluids* 146, 105–116.
- [37] Harten, A., Engquist, B., Osher, S., Chakravarthy, S.R., 1987. Uniformly high order accurate essentially non-oscillatory schemes, III. *Journal of Computational Physics* 71, 231–303.
- [38] Harten, A., Lax, P.D., Leer, B.v., 1983. On upstream differencing and Godunov-type schemes for hyperbolic conservation laws. *SIAM review* 25, 35–61.
- [39] Hu, C., Shu, C.W., 1999. Weighted essentially non-oscillatory schemes on triangular meshes. *Journal of Computational Physics* 150, 97–127.
- [40] Huynh, H.T., . A flux reconstruction approach to high-order schemes including discontinuous galerkin methods, in: 18th AIAA Computational Fluid Dynamics Conference, p. 4079.

- [41] Jiang, G.S., Shu, C.W., 1996. Efficient Implementation of Weighted ENO Schemes. *Journal of Computational Physics* 126, 202–228.
- [42] Johnsen, E., Larsson, J., Bhagatwala, A.V., Cabot, W.H., Moin, P., Olson, B.J., Rawat, P.S., Shankar, S.K., Sjögreen, B., Yee, H., Zhong, X., Lele, S.K., 2010. Assessment of high-resolution methods for numerical simulations of compressible turbulence with shock waves. *Journal of Computational Physics* 229, 1213–1237.
- [43] Krank, B., Kronbichler, M., Wall, W.A., 2019. A multiscale approach to hybrid RANS/LES wall modeling within a high-order discontinuous Galerkin scheme using function enrichment. *International Journal for Numerical Methods in Fluids* 90, 81–113.
- [44] Lefieux, J., Garnier, E., Sandham, N., 2019. DNS Study of Roughness-Induced Transition at Mach 6, in: *AIAA Aviation 2019 Forum*, p. 3082.
- [45] LeVeque, R.J., 1996. High-resolution conservative algorithms for advection in incompressible flow. *SIAM Journal on Numerical Analysis* 33, 627–665.
- [46] Levy, D., Puppo, G., Russo, G., 1999. Central WENO schemes for hyperbolic systems of conservation laws. *ESAIM: Mathematical Modelling and Numerical Analysis-Modélisation Mathématique et Analyse Numérique* 33, 547–571.
- [47] Levy, D., Puppo, G., Russo, G., 2000. Compact central WENO schemes for multidimensional conservation laws. *SIAM Journal on Scientific Computing* 22, 656–672.
- [48] Li, W., Ren, Y.X., 2012. The multi-dimensional limiters for solving hyperbolic conservation laws on unstructured grids II: extension to high order finite volume schemes. *Journal of Computational Physics* 231, 4053–4077.
- [49] Liu, X.D., Osher, S., Chan, T., 1994. Weighted Essentially Non-oscillatory Schemes. *Journal of Computational Physics* 115, 200–212.

- [50] Liu, Y., Zhang, Y.T., 2013. A robust reconstruction for unstructured WENO schemes. *Journal of Scientific Computing* 54, 603–621.
- [51] Lusher, D.J., Sandham, N., 2019. Assessment of low-dissipative shock-capturing schemes for transitional and turbulent shock interactions, in: *AIAA Aviation 2019 Forum*, p. 3208.
- [52] Lusher, D.J., Sandham, N.D., 2020. Shock-wave/boundary-layer interactions in transitional rectangular duct flows. *Flow, Turbulence and Combustion* 105, 649–670.
- [53] Michalak, C., Ollivier-Gooch, C., 2009. Accuracy preserving limiter for the high-order accurate solution of the Euler equations. *Journal of Computational Physics* 228, 8693–8711.
- [54] Motheau, E., Wakefield, J., 2020. Investigation of finite-volume methods to capture shocks and turbulence spectra in compressible flows. *Communications in Applied Mathematics and Computational Science* 15, 1–36.
- [55] Ollivier-Gooch, C., Van Altena, M., 2002. A high-order-accurate unstructured mesh finite-volume scheme for the advection–diffusion equation. *Journal of Computational Physics* 181, 729–752.
- [56] Pirozzoli, S., 2011. Numerical methods for high-speed flows. *Annual Review of Fluid Mechanics* 43, 163–194.
- [57] Renac, F., de la Llave Plata, M., Martin, E., Chapelier, J.B., Couaillier, V., 2015. Aghora: a high-order DG solver for turbulent flow simulations, in: *IDIHOM: Industrialization of High-Order Methods-A Top-Down Approach*. Springer, pp. 315–335.
- [58] Ryu, D., Jones, T.W., Frank, A., 2000. The magnetohydrodynamic Kelvin-Helmholtz instability: A three-dimensional study of nonlinear evolution. *The Astrophysical Journal* 545, 475.
- [59] San, O., Kara, K., 2015. Evaluation of Riemann flux solvers for WENO reconstruction schemes: Kelvin–Helmholtz instability. *Computers & Fluids* 117, 24–41.

- [60] Shi, J., Hu, C., Shu, C.W., 2002. A Technique of Treating Negative Weights in WENO Scheme. *Journal of Computational Physics* 175, 108–127.
- [61] Shu, C.W., 1987. TVB uniformly high-order schemes for conservation laws. *Mathematics of Computation* 49, 105–121.
- [62] Shu, C.W., 2003. High-order finite difference and finite volume WENO schemes and discontinuous Galerkin methods for CFD. *International Journal of Computational Fluid Dynamics* 17, 107–118.
- [63] Shu, C.W., 2009. High order weighted essentially nonoscillatory schemes for convection dominated problems. *SIAM review* 51, 82–126.
- [64] Shu, C.W., Osher, S., 1989. Efficient implementation of essentially non-oscillatory shock-capturing schemes, ii. *Journal of Computational Physics* 83, 32–78.
- [65] Sun, Z., Inaba, S., Xiao, F., 2016. Boundary Variation Diminishing (BVD) reconstruction: A new approach to improve Godunov schemes. *Journal of Computational Physics* 322, 309–325.
- [66] Titarev, V., Tsoutsanis, P., Drikakis, D., 2010. WENO schemes for mixed-element unstructured meshes. *Communications in Computational Physics* 8, 585.
- [67] Toro, E.F., 2013. *Riemann solvers and numerical methods for fluid dynamics: a practical introduction*. Springer Science & Business Media.
- [68] Toro, E.F., Spruce, M., Speares, W., 1994. Restoration of the contact surface in the HLL-Riemann solver. *Shock waves* 4, 25–34.
- [69] Tsoutsanis, P., 2018. Extended bounds limiter for high-order finite-volume schemes on unstructured meshes. *Journal of Computational Physics* 362, 69–94.
- [70] Tsoutsanis, P., 2019. Stencil selection algorithms for WENO schemes on unstructured meshes. *Journal of Computational Physics: X* 4, 100037.

- [71] Tsoutsanis, P., Antoniadis, A.F., Drikakis, D., 2014. WENO schemes on arbitrary unstructured meshes for laminar, transitional and turbulent flows. *Journal of Computational Physics* 256, 254–276.
- [72] Tsoutsanis, P., Antoniadis, A.F., Jenkins, K.W., 2018. Improvement of the computational performance of a parallel unstructured WENO finite volume CFD code for Implicit Large Eddy Simulation. *Computers & Fluids* 173, 157–170.
- [73] Tsoutsanis, P., Titarev, V.A., Drikakis, D., 2011. WENO schemes on arbitrary mixed-element unstructured meshes in three space dimensions. *Journal of Computational Physics* 230, 1585–1601.
- [74] Van Leer, B., 1974. Towards the ultimate conservative difference scheme. ii. monotonicity and conservation combined in a second-order scheme. *Journal of computational physics* 14, 361–370.
- [75] Van Leer, B., 1977. Towards the ultimate conservative difference scheme. IV. A new approach to numerical convection. *Journal of computational physics* 23, 276–299.
- [76] Van Leer, B., 1979. Towards the ultimate conservative difference scheme. V. A second-order sequel to Godunov’s method. *Journal of computational Physics* 32, 101–136.
- [77] Vandenhoeck, R., Lani, A., 2019. Implicit High-Order Flux Reconstruction Positivity Preserving LLAV Scheme for Viscous High-Speed Flows, in: *AIAA Scitech 2019 Forum*, p. 1153.
- [78] Venkatakrisnan, V., 1995. Convergence to steady state solutions of the Euler equations on unstructured grids with limiters. *Journal of computational physics* 118, 120–130.
- [79] Witherden, F., Vincent, P., Jameson, A., 2016. High-order flux reconstruction schemes, in: *Handbook of numerical analysis*. Elsevier. volume 17, pp. 227–263.

- [80] Woodward, P., 1984. The numerical simulation of two-dimensional fluid flow with strong shocks. *Journal of Computational Physics* 54, 115–173.
- [81] Zhang, H., Zhang, F., Liu, J., McDonough, J., Xu, C., 2020. A simple extended compact nonlinear scheme with adaptive dissipation control. *Communications in Nonlinear Science and Numerical Simulation* 84, 105191.
- [82] Zhang, H., Zhang, F., Xu, C., 2019. Towards optimal high-order compact schemes for simulating compressible flows. *Applied Mathematics and Computation* 355, 221–237.
- [83] Zhang, Y.T., Shu, C.W., 2009. Third order WENO scheme on three dimensional tetrahedral meshes. *Communications in Computational Physics* 5, 836–848.
- [84] Zhao, G.Y., Sun, M.B., Pirozzoli, S., 2020. On shock sensors for hybrid compact/WENO schemes. *Computers & Fluids* 199, 104439.
- [85] Zhou, T., Li, Y., Shu, C.W., 2001. Numerical comparison of WENO finite volume and Runge–Kutta discontinuous Galerkin methods. *Journal of Scientific Computing* 16, 145–171.
- [86] Zhu, J., Qiu, J., 2016. A new fifth order finite difference WENO scheme for solving hyperbolic conservation laws. *Journal of Computational Physics* 318, 110–121.
- [87] Zhu, J., Shu, C.W., 2019. A new type of multi-resolution WENO schemes with increasingly higher order of accuracy on triangular meshes. *Journal of Computational Physics* 392, 19–33.
- [88] Zhu, J., Shu, C.W., 2020. A new type of third-order finite volume multi-resolution WENO schemes on tetrahedral meshes. *Journal of Computational Physics* 406, 109212.